



HAL
open science

Landscape evolution associated with the 2014–2015 Holuhraun eruption in Iceland

Léa Bonnefoy, C.W. Hamilton, S.P. Scheidt, S. Duhamel, A. Höskuldsson, I.
Jónsdóttir, T. Thordarson, U. Münzer

► **To cite this version:**

Léa Bonnefoy, C.W. Hamilton, S.P. Scheidt, S. Duhamel, A. Höskuldsson, et al.. Landscape evolution associated with the 2014–2015 Holuhraun eruption in Iceland. *Journal of Volcanology and Geothermal Research*, 2019, 387 (1 December 2019), pp.art. 106652. 10.1016/j.jvolgeores.2019.07.019 . insu-02262355

HAL Id: insu-02262355

<https://insu.hal.science/insu-02262355>

Submitted on 20 Jul 2022

HAL is a multi-disciplinary open access archive for the deposit and dissemination of scientific research documents, whether they are published or not. The documents may come from teaching and research institutions in France or abroad, or from public or private research centers.

L'archive ouverte pluridisciplinaire **HAL**, est destinée au dépôt et à la diffusion de documents scientifiques de niveau recherche, publiés ou non, émanant des établissements d'enseignement et de recherche français ou étrangers, des laboratoires publics ou privés.



Distributed under a Creative Commons Attribution - NonCommercial 4.0 International License

1 **Landscape evolution associated with the 2014–2015 Holuhraun eruption in Iceland**

2

3 L.E. Bonnefoy^{1,2}, C.W. Hamilton³, S.P. Scheidt⁴, S. Duhamel⁵, Á. Höskuldsson⁶, I.

4 Jónsdóttir⁶, T. Thordarson⁶, and U. Münzer⁷

5

6 ¹ Laboratoire d'Etudes Spatiales et d'Instrumentation en Astrophysique (LESIA), Observatoire

7 de Paris-Meudon, LESIA (Bât. 18), 5, place Jules Janssen, 92195 Meudon Cedex,

8 France

9 ² Laboratoire Atmosphères, Milieux, Observations Spatiales (LATMOS), UVSQ/CNRS/Paris

10 VI, UMR 8190, 78280 Guyancourt, France

11 ³ Lunar and Planetary Laboratory, University of Arizona, 1629 E. University Blvd., Tucson,

12 AZ 85721, USA

13 ⁴ Planetary Science Institute, 1700 East Fort Lowell, Suite 106, Tucson, AZ 85719, USA

14 ⁵ Lamont-Doherty Earth Observatory, Division of Biology and Paleo Environment, P.O. Box

15 1000, 61 Route 9W, Palisades, NY 10964, USA

16 ⁶ Faculty of Earth Sciences, University of Iceland, Sturlugarta 7, 101 Reykjavík, Iceland

17 ⁷ Ludwig-Maximilians-University Munich, Department of Earth and Environmental

18 Sciences, Section Geology, Luisenstr. 37, 80333 Munich, Germany

19

20 **Abstract:**

21 The 2014–2015 Holuhraun eruption in Iceland developed between the outlet glacier

22 Dyngjufökull and the Askja central volcano and extruded a bulk lava volume of over 1 km³

23 onto the floodplain of the Jökulsá á Fjöllum river, making it the largest effusive eruption in

24 Iceland during the past 230 years. Time-series monitoring using a combination of traditional

25 aerial imaging, unmanned aerial systems, and field-based geodetic surveys, established an

26 unprecedented record of the hydrological response of the river system to this lava flow. We
27 observed: (1) the formation of lava-dammed lakes and channels produced during dam-
28 breaching events; (2) percolation of glacial meltwater into the porous and permeable lava,
29 forming an ephemeral hydrothermal system that included hot pools and hot springs that
30 emerged from the lava flow front; and (3) the formation of new seepage channels caused by
31 upwelling of water around the periphery of the lava flow. The observations show that lava
32 flows, like the one produced by the 2014–2015 Holuhraun eruption, can cause significant
33 hydrological changes that continue for several years after the lava is emplaced. Documenting
34 these processes is therefore crucial for our interpretation of volcanic landscapes and processes
35 of lava–water interaction on both Earth and Mars.

36

37 **1. Introduction**

38 Effusive volcanic activity is one of the dominant processes shaping the surface of the
39 Earth and other planetary bodies (Self et al., 1998). Eruptions generating $\geq 1 \text{ km}^3$ Dense Rock
40 Equivalent (DRE) of lava only occur in Iceland every few hundred years (Thordarson and
41 Höskuldsson, 2008). The infrequency of these events makes it difficult to fully understand
42 their consequences in terms of landscape evolution. The 2014–2015 Holuhraun eruption
43 provides us with the first opportunity to directly monitor processes of landscape evolution
44 associated with a basaltic lava flow of this magnitude in an analog environment for sandsheets
45 on the surface of Mars (Dundas et al., 2017; Sara, 2017; Sara et al., 2017).

46 After a brief precursor event on August 29, 2014, the main phase of the effusive
47 eruption began on August 31, 2014 and lasted until February 27, 2015, covering an area of
48 83.53 km^2 (Pedersen et al., 2017; Voigt et al., 2017, 2018). There are several estimates of the
49 bulk lava volume emplaced during this ~6-month period, ranging from $1.44 \pm 0.07 \text{ km}^3$ to 1.8
50 $\pm 0.2 \text{ km}^3$ (e.g., Gudmundsson et al., 2016; Höskuldsson et al., 2016; Jaenicke et al., 2016;

51 Münzer et al., 2016; Dirscherl and Rossi, 2018; Bonny et al., 2018). Converted to DRE,
52 volume estimates range from 1.21 km³ (Bonny et al., 2018) to 1.36 ± 0.07 km³ (Dirscherl and
53 Rossi, 2018), but these DRE values may have been overestimated because they do not take
54 into account macroscale porosity between the lava blocks forming the crustal carapace of the
55 flow. This makes the 2014–2015 eruption at Holuhraun the largest outpouring of lava in
56 Iceland since the 1783–1784 Laki eruption (14.7 km³ DRE; Thordarson and Self, 1993). The
57 lava partially covers the Dyngjúsandur outwash plain where the river Jökulsá á Fjöllum
58 originates (Arnalds et al., 2016; Pedersen et al., 2017) as well as two older Holuhraun lava
59 flows erupted in 1792 and 1867 and Askja lava flows erupted in 1924–1929 (Hartley and
60 Thordarson, 2013; Hartley et al., 2016). The eruption was preceded by a laterally propagating
61 earthquake swarm (Sigmundsson et al., 2015; Gudmundsson et al., 2016) and three small
62 subglacial eruptions (Reynolds et al., 2017). It was also accompanied by graben subsidence
63 (Hjartardóttir et al., 2016; Ruch et al., 2016), sulfur outgassing (Gíslason et al., 2015;
64 Ilyinskaya et al., 2017), and simultaneous subsidence in the Barðarbunga caldera
65 (Gudmundsson et al., 2016; Rossi et al., 2016; Dirscherl and Rossi, 2018).

66 The time-series dataset presented in this study reveals both catastrophic and
67 continuous hydrological changes in the vicinity of the 2014–2015 Holuhraun lava flow.
68 Observations of these events are important for understanding lava-induced changes in
69 hydrologic activity on Earth and for interpreting those preserved within the geological record
70 of Mars. For instance, lava-induced hydrothermal systems have the potential to generate
71 habitable environments for extremophile life (Baratoux et al., 2011; Cousins et al., 2013) and
72 observation of groundwater seepage near a lava flow may provide some insight into the
73 possibility of Martian seepage channels (Baker et al., 1990, 2015; Goldspiel and Squyres,
74 2000). Additionally, the implications for geological hazard mitigation, especially relating to

75 the formation and breaching of lava-dammed lakes could have significant impacts in
76 populated areas.

77 In this study, we provide an overview of the 2014–2015 Holuhraun eruption, as well
78 as the processes leading to the formation of theater-headed channels by seepage erosion. We
79 then summarize the characteristics of aerial images and topography obtained before the
80 eruption (summers of 2003 and of 2013) and during the summers of 2015, 2016, 2017, and
81 2018. These remote sensing data are combined with yearly field measurements of key water
82 characteristics and with daily summer eyewitness observations of the area of interest by the
83 authors or the Vatnajökull National Park rangers. Landscape evolution processes observed
84 include the development and modification of hot springs emerging from the lava, the
85 development of seepage channels near the lava flow margin, and changes in the structure of
86 river channels from year to year linked to the formation and collapse of a lava-dammed lake
87 in 2016. Comparing the changes brought about by catastrophic processes (i.e., dam-breaching
88 events) and continuous processes (e.g., seepage erosion) suggests that the two have different,
89 but comparably important effects on landscape evolution after the deposition of a lava flow.
90 This result, beyond being applicable to our understanding of fluvio-volcanic processes on
91 Earth, also has implications for Mars, where both floods and groundwater seepage may have
92 been major agents of surface change, especially as linked to volcanic events.

93

94 **2. Background**

95 **2.1. Influences of basaltic lava flow emplacement on hydrology**

96 Lava flows tend to occupy topographic lows, and often encounter river drainage
97 systems. Lava-dammed lakes associated with low viscosity basaltic lavas are found
98 throughout the world (e.g., Lowe and Green, 1987; Huscroft et al., 2004; Roach et al., 2008;
99 Allen et al., 2011; Ely et al., 2012). For example, the 1719–1721 eruption at Wudalianchi,

100 China formed five lava-dammed lakes (Feng and Whitford-Stark, 1986). However, if the
101 topography permits it, the river may instead change its course, often by following the
102 boundary of the lava flow field, as in the case of 1783–1784 Laki lava flow field (Thordarson
103 and Self, 1993; Thordarson et al., 2003), the Snake River in Idaho (Stearns, 1936), and the
104 McKenzie River in Oregon (Deligne, 2012).

105 Basaltic lava flows also affect groundwater systems. Solidified basalt lava has a high
106 porosity and permeability, due to the presence of vesicles, cooling-contraction joints, and lava
107 tubes. Subaerial basaltic lava flows therefore tend to transport surface water into aquifers,
108 leading to very little surface runoff as streams and lakes disappear into the basalt (Stearns,
109 1942). Lava-dammed lakes often use the lava itself as an outlet, as in Clear Lake, Oregon
110 (Deligne, 2012). The aquifers developed in basalt can be extensive and lead to the formation
111 of springs along their margins, as has been observed for example in the Snake River Plain in
112 Idaho (Stearns, 1936) as well as in young lava flows in Iceland and Australia (Kiernan et al.,
113 2003). However, the permeability of basalt decreases with time, causing groundwater flow to
114 eventually be replaced by surface flow (Stearns, 1942; Jefferson et al., 2010). This is
115 particularly true for lava in proglacial sandsheets (i.e. the equivalent of sandur plains in
116 Iceland), where regular flooding transports fine material into the lava, thus filling pores and
117 decreasing its permeability. The 2014–2015 Holuhraun lava flow field provides the first
118 opportunity to monitor how the groundwater system reacts to a large lava flow.

119

120 **2.2. Local geological context**

121 Our study area extends from the Dyngjufökull outlet glacier of Vatnajökull to Askja,
122 and encompasses the region covered by the 2014–2015 Holuhraun lava flow field (Fig. 1).
123 The new flow field overlies a proglacial sandsheet (Mountney and Russel, 2004), which
124 typically is covered in snow from September/October to May/June, and then partially flooded

125 on a diurnal basis during the summer by glacial meltwater (Bahr, 1997; Maizels, 2002;
126 Arnalds et al., 2016). The glacial outwash sediment, deposited by episodic flooding and
127 possibly also by glacial outburst floods (“jökulhlaups” in Icelandic), provides source material
128 to the Dyngjusandur sandsheet (Mountney and Russell, 2004; Alho et al., 2005; Baratoux et
129 al., 2011; Sara, 2017; Baldursson et al., 2018). Tributaries to the Jökulsá á Fjöllum that flood
130 the outwash plain are banked on the north side by older lava flows erupted from the Askja
131 volcanic system in the north, from the Bárðarbunga–Veiðivötn system in the west and from
132 the Kverkfjöll system in the east; the youngest of these are mapped in Fig. 2. The northern
133 part of the sandsheet thus includes a succession of lava flows from the Askja volcano, the
134 youngest of which was formed between 1924 and 1929 (Hartley et al., 2016). The three
135 Holuhraun lava flow fields are located in the southern part of the sandsheet (i.e., closer to the
136 Vatnajökull ice cap) and include the flow fields formed in 1797 and 1867. These two flow
137 fields originated from separate 1 to 2-km long fissure segments that trend just east of north
138 and are situated close to the southern terminus of Askja fissure swarm (Hartley and
139 Thordarson, 2013). The 2014–2015 eruption reactivated the 1867 fissure segment, generating
140 new vents superimposed on the 1867 vents, erupting lava onto Dyngjusandur and covering
141 part of the Jökulsá á Fjöllum riverbed (e.g., Ruch et al 2016; Pedersen et al 2017; Eibl et al
142 2017; Fig. 2).

143 The dominant hydrological features within the region of interest include outlet glaciers
144 from Vatnajökull, the Jökulsá á Fjöllum and the surrounding floodplain (i.e., Dyngjusandur),
145 a lake (Dyngjuvatn), and numerous seepage channels. Lake Dyngjuvatn, located between
146 Askja and the small interglacial shield volcano Vaðalda, is fed mainly by seasonal melt from
147 Askja and has no outlet (Graettinger et al., 2013). Instead, water either drains into the ground
148 or evaporates throughout the summer, leaving it mostly dry by the time snowfall begins again.
149 At the Upptyppingar gauging station in the Jökulsá á Fjöllum (Fig. 1), 98.1% of the river

150 discharge comes from a combination of springs and glacial melt (Esther Hlíðar Jensen,
151 personal communication, 2018). This indicates that runoff from precipitation is a negligible
152 source of water in the Holuhraun lava field. The glacial water contributing to the Jökulsá á
153 Fjöllum discharge at Upptyppingar comes from the Dyngjujökull and Kverkfjöll outlet
154 glaciers. Most of the water flowing across Dyngjusandur and around and through the 2014–
155 2015 Holuhraun lava is from Dyngjujökull, while the streams from Kverkfjöll take a slightly
156 more eastern course. The springwater contribution to the Jökulsá á Fjöllum includes a large
157 seepage channel called Svartá, which is fed by a shallow aquifer system. The Svartá seepage
158 channel emerges to the northeast of the 2014–2015 Holuhraun lava flow field and forms a
159 small stream system that runs along the edge of the Vaðalda shield volcano for about 900 m
160 before reaching the Jökulsá á Fjöllum (Fig. 1).

161 Prior to the 2014–2015 eruption, the braided streams covering much of Dyngjusandur
162 over the summers supplied water into the Jökulsá á Fjöllum. Small seepage channels were
163 also common near the banks of the Jökulsá á Fjöllum about 20 km downstream from the
164 Dyngjujökull glacier (e.g., Fig. 6a). During the winter, springs with a nearly constant
165 discharge of about 20 m³/s, similar to that of Svartá, emerged within the riverbed (Baldursson
166 et al., 2018). Thus, where Svartá merges with the Jökulsá á Fjöllum at the foot of Vaðalda,
167 both streams had comparable winter fluxes of about 20 m³/s. After this point, the river is fed
168 by more small springs in winter and glacial meltwater in summer. The winter (October to
169 April) discharge measured at Upptyppingar was usually 55–60 m³/s, whereas the average
170 August discharge measured between 1972 and 2015 was around 200 m³/s (Gylfadóttir, 2016).
171 Thus during the winter, springwater provides the main contribution to the Jökulsá á Fjöllum at
172 Upptyppingar; while during summer, most of the water is supplied by glacial melt.

173 The regional topographic slope and orientation of the Askja fissure swarm likely exert
174 strong controls on the groundwater flow directions in the vicinity of the 2014–2015

175 Holuhraun lava flow field (Baldursson et al., 2018). However, to the north groundwater flow
176 patterns may be complicated by surface runoff and seasonal meltwater contributions from the
177 Askja massif and Vaðalda lava shield.

178

179 **2.3. The 2014–2015 Holuhraun eruption**

180 The 2014–2015 Holuhraun eruption was preceded by an intense earthquake swarm
181 that was detected along the SE margins of the 10-km-diameter Bárðarbunga caldera on
182 August 16, 2014. The propagation of this seismic swarm has been interpreted as the
183 movement of magma through a dike 45 km toward the northeast (Sigmundsson et al., 2015).
184 When the magma reached the surface in Dyngjusandur, about 7 km north of the Dyngjujökull
185 outlet glacier of Vatnajökull, it became a fissure eruption. The first phase of the eruption
186 lasted 4 hours on August 29, 2014 (Sigmundsson et al., 2015). It is possible that several small
187 eruptions took place underneath the Vatnajökull glacier, as indicated by the development of
188 “ice cauldrons”, which are circular depressions formed in ice surface by melting of the base of
189 the ice (e.g. Reynolds et al 2017). The main phase of the eruption lasted from August 31,
190 2014 to February 27, 2015, producing a lava flow field covering an area of approximately
191 83.53 km². A visible graben with vertical displacement up to 5 m formed around the erupting
192 vents during the early stages (the first three days) of the eruption (Hjartardóttir et al., 2016;
193 Ruch et al., 2016). Though the eruption generated considerable sulfur outgassing, its
194 environmental impact was largely mitigated by the weak eruption intensity, the low (typically
195 <4 km) eruption plumes, and the remoteness of the area in the sparsely vegetated highlands
196 (e.g. Gíslason et al., 2015). During this time a gradual subsidence was observed of the
197 Bárðarbunga caldera (e.g. Gudmundsson et al., 2016; Dirscherl and Rossi, 2017).

198 A unique aspect of the eruption was that its lava flows encountered the Jökulsá á
199 Fjöllum, Iceland’s highest discharge river, on September 7, 2014, and then proceeded to cover

200 part of the riverbed, causing a reorganization of the fluvial system within the region. The
201 landscape before and after the eruption is shown in Fig. 2. Initially, the lava was bounded by
202 the riverbanks and the Askja 1924–1929 flow field, but subsequent breakouts covered these
203 boundaries (Pedersen et al., 2017; Kolzenburg et al., 2018). While explosive water–lava
204 interactions were observed on September 8, 2014, no explosive constructs were formed
205 (Pedersen et al., 2017). At the distal (east) end of the lava flow field, lava-induced
206 hydrothermal activity formed hot springs, which were still warm (10.7°C) in the summer of
207 2018. Herein, we refer to this locality as the “hot springs region” (Fig. 3). The deposition of
208 lava within the riverbed also led to the development of two lava-dammed lakes, which we
209 refer here to as the “western lake” and “eastern lake” (Fig. 3). The streams feeding the lava-
210 dammed lakes originate from different parts of the glacier and are separated by the older
211 Holuhraun lava flow fields. These two streams were already separate before the 2014–2015
212 eruption (e.g., Figs. 1 and 2). In 2016, the eastern lake breached through to the hot springs
213 region; this event is described in detail in Section 4.3. After July 22, 2016, glacial stream
214 water and water from the hot springs merged to produce braided network streams with a wide
215 range of temperatures.

216

217 **2.4. Seepage channels**

218 In the region of interest, the Jökulsá á Fjöllum is fed not only by glacial melt, but also
219 by seepage springs, such as Svartá (Fig. 4), which is an archetypal example of a seepage
220 channel formed within unconsolidated sediment (Woodruff and Gergel, 1969; Higgins et al.,
221 1982). Non-artesian springs form when the groundwater table intersects with the surface,
222 leading to the formation of a stream. In unconsolidated sediment, as within Dyngjusandur,
223 groundwater sapping erodes the base of the channel, creating an overhang and eventually
224 leading to a collapse of the headwall. The term “sapping” designates the erosion of the base of

225 a scarp causing the creation of an overhang (Dunne, 1990; Lamb et al., 2006; Pelletier and
226 Baker, 2011). The collapsed sediment is then evacuated by the flowing stream (Schorghofer et
227 al., 2004). Seepage channels therefore grow by headward erosion and form characteristic
228 theater-shaped heads (Fig. 4; Higgins, 1982; Dunne, 1990). As the individual channels grow,
229 groundwater flow converges to the channel head, increasing headward erosion (Dunne, 1980;
230 Baker et al., 1990). The Svartá theater-shaped channel heads are up to 10 m high and are
231 formed of steep slip faces of sand (Mountney and Russel, 2004). Mountney and Russell
232 (2004) report seeing 1–2-m-wide slabs of sand sliding down the slip face due to sapping
233 eroding its base. They also report the presence of a pebbly gravel layer at the base of the slip
234 faces and it is likely that much of the groundwater flow occurs within this gravel layer.

235

236 **3. Methodology**

237 **3.1. Aerial data**

238 To monitor the hydrology of the region, we compare high-resolution imagery and
239 topography from different sources at five time periods, one before the eruption (2003/2013)
240 and four after the eruption, during the summers of 2015, 2016, 2017, and 2018. In each case,
241 observations were collected in the summer months using traditional aircraft and small
242 unmanned aerial systems (sUAS). The highest resolution datasets are obtained during our
243 field campaigns in 2015, 2016, 2017, and 2018 using sUAS. These data include 5–20
244 cm/pixel stereo-derived digital terrain models (DTMs) and 1–4 cm/pixel orthomosaics
245 covering 21% of the flow, including repeat imagery of several regions in 2015, 2016, 2017,
246 and 2018 (Voigt et al., 2017, 2018). To investigate hydrological changes associated with the
247 Holuhraun lava flow field, we focus on a subset of these data, obtained at the distal northern
248 end of the field where hot springs emerge from a flow front (Fig. 3). The datasets used in this
249 study are described further in Table A1 and in Sections 3.1.1–3.1.4; the location of

250 subsequent figures is given in Fig. 5. The 2015–2018 sUAS datasets used are being made
251 publicly available on the University of Arizona Geospatial Repository Portal.

252

253 **3.1.1. Pre-emplacment datasets (2003–2014)**

254 The pre-emplacment DTM and orthomosaic were acquired and processed by Loftmyndir ehf.
255 from airborne photogrammetry datasets taken on August 12, 2013 over most of the region and
256 on August 23, 2003 in the hot springs region. The DTM was generated by combining datasets
257 and smoothing the seams. The spatial resolution of the DTM is 5 m/pixel, and estimated 1
258 sigma error bars in elevation vary from ± 0.5 m to ± 5 m (Appendix A). The orthoimage has a
259 spatial resolution of 50 cm/pixel. The Environmental Systems Research Institute (Esri)
260 ArcGIS World imagery basemap, which is a combination of multiple datasets (sources: Esri,
261 DigitalGlobe, GeoEye, i-cubed, USDA FSA, USGS, AEXm Getmapping, AeroGRID, IGN,
262 IGP, Swisstopo, and the GIS user community), was also used to provide regional context.

263

264 **3.1.2. The 2015 dataset**

265 The 2015 regional DTM (Appendix A, Fig. A1) uses a combination of datasets to
266 obtain the best possible quality of data over the whole region. LiDAR data, collected and
267 processed by the Natural Environment Research Council (NERC) was acquired on September
268 4, 2015, and had at this time the highest spatial (2 m/pixel) and vertical (mean error of 4 to 5
269 cm depending on the flight line) resolution over the majority of the lava flow. Eight flights
270 lines were made over the Holuhraun lava flow field: seven of these are parallel and aligned
271 with the long axis of the field (from the vent to the hot springs region) while the eighth is
272 transverse and crosses all the others. The LiDAR therefore does not cover the entirety of the
273 flow field. Furthermore, a small cloud and fumeroles obscured parts of the lava, and created
274 gaps in the data. Where LiDAR data was unavailable, we used another photogrammetry-

275 derived DTM provided by Loftmyndir ehf. using data taken on August 30, 2015. Where
276 clouds obscured interior parts of the 2014–2015 Holuhraun flow field, occluded regions were
277 masked and interpolated using Loftmyndir ehf. data. Where clouds covered the edge of the
278 flow, contour lines were interpolated using Esri ArcGIS editing tools for every meter using
279 the orthoimage as reference. The post-emplacement imagery includes the 50 cm/pixel August
280 30, 2015 orthoimage provided by Loftmyndir ehf., as well as a 20 cm/pixel true
281 orthophotomosaic derived from UltraCam-Xp airborne data (captured on September 8, 2015)
282 and provided through the IsViews project (Ludwig-Maximilians-University of Munich).
283 During the 2015 field campaign, sUAS image observations were also made in selected
284 regions using two DJI Phantom 3 Pro quadcopters, each equipped with a 12 MP image
285 camera. With a flight altitude of 100 meters, a ground sampling distance (GSD) of 4 cm per
286 pixel is achieved. Image data were imported into the software package Pix4Dmapper Pro to
287 produce orthoimages and DTMs. A DTM produced from image data with a 4 cm GSD has a
288 spatial resolution of 16 cm per pixel. Ground control points (GCPs) were placed in the field
289 and surveyed using a Trimble R10 differential global positioning system (dGPS). Although
290 the sUAS has GPS for navigation, its accuracy and precision is low. The R10 dGPS is capable
291 of producing survey points with excellent precision (0.8 cm horizontal and 1.5 cm vertical);
292 therefore, these survey points were used in Pix4Dmapper Pro to accurately georeference
293 orthoimages and DTMs. In addition to GCPs, Phantom sUAS surveys were co-registered to
294 high spatial resolution data products (2016 orthoimages and DTMs) produced by
295 differentially corrected UX5-HP surveys (described below in section 3.1.3).

296

297 **3.1.3. The 2016, 2017, and 2018 datasets**

298 During our field campaigns in August of 2016, 2017, and 2018, sUAS data were
299 obtained over the 2014–2015 Holuhraun lava flow field. All 2016 and 2018 image data were

300 acquired using a Trimble UX5-HP fixed-wing unmanned aircraft (Cosyn and Miller, 2013;
301 Pauly, 2016). This sUAS has a dedicated GPS for autonomous navigation as well as a
302 separate dGPS receiver for recording a raw GPS data stream. During UX5-HP flights, a base
303 station continuously records raw GPS data as well. In post-processing in Trimble Business
304 Center, the base station and fixed-wing GPS data are used to calculate the positions of the
305 plane at the exact instances of image acquisition from a Sony a7R camera. Images are 36 MP
306 and capture exceptional detail of the ground surface. Because each image is accurately
307 georeferenced and combined with camera pointing information using the UX5-HP's inertial
308 measurement unit (IMU), GCPs are not needed to complete an accurate and precise
309 stereophotogrammetric survey. Image data in 2017 were taken using a DJI Phantom 4 Pro
310 quadcopter and was processed into DTMs and orthoimages using Pix4Dmapper Pro. These
311 data were co-registered to common ground targets and features seen in the 2016 UX5-HP
312 orthoimage and DTM. The 2016 and 2017 data is concentrated on the hot springs region and
313 the eastern lava-dammed lake.

314

315 **3.2. Mapping**

316 Maps were constructed at three scales and include: (1) a context map depicting the
317 pre-eruption hydrology (Fig. 1); (2) two regional maps focused on the landscape directly
318 around the 2014–2015 Holuhraun lava flow field (Fig. 2), and (3) five detailed maps of the
319 hot springs region illustrating annual changes (Fig. 6). All mapping was completed using
320 ArcGIS software by Esri.

321 The pre-eruption hydrological context map (Fig. 1) shows surface water features and
322 the lava flow outline. This map covers 2,190 km² and was digitized at a scale of 1:25,000
323 using the pre-emplacement Loftmyndir ehf. orthomosaics and ArcMap basemap images.

324 The regional maps (Fig. 3) show the 2014–2015 Holuhraun lava flow field and its
325 immediate surroundings, both before (in 2003 and 2013) and after (in 2015) the eruption.
326 Here, we also show the 2014–2015 Holuhraun lava flow field outline, and to establish
327 geological context, we included other lava flow fields in the region with ages less than 300
328 years as well as riverbeds that were active in 2003/2013 and 2015. However, the position of
329 the Jökulsá á Fjöllum tributaries flowing through the flood plain varies daily over the summer.
330 These streams are often only centimeters to tens of centimeters deep and, as they flow over
331 the highly permeable ground, they are often absorbed before they reach the main riverbed. We
332 therefore rely primarily on the topographic boundaries to map the extent of channels hosting
333 the braided stream system. The two maps in Fig. 3 each cover 165 km² and were digitized at a
334 scale of 1:2,000 using the pre-emplacement and 2015 datasets described above.

335 Maps of the hot springs region (Fig. 6) were developed for 2003, 2015, 2016, 2017,
336 and 2018. These maps focus on the different sources of water, which were identified with the
337 following definitions, using stream color, morphology, temperature, and flow directions.
338 “Heated water” corresponds to warm (>8°C) water, which emerges from the lava and has a
339 blue or green color due to the presence of sulfates and algae. “Glacial water” can be traced
340 back to the Dyngjujökull outlet glacier on the northern part of Vatnajökull ice cap. While rain
341 and groundwater contribute to these streams, the main source of the water is glacial melt from
342 the glacier. “Glacial water” has high turbidity and is milky white in color due to the
343 entrainment of fine particles. “Spring water” streams are identified by being sourced directly
344 out of the ground, and are clear water, filtered by the sand and rock. “Spring water” channel
345 heads often have the theater-headed morphology characteristic of seepage channels (see Fig.
346 4). Where two different types of water meet in one stream, we use both colors, with the width
347 of each color approximately representing the contribution of each water source (this can vary
348 during the day with the glacial river water levels). Finally, we refined the lava flow outline in

349 the hot springs region for each year to account for the rising and lowering of the surrounding
350 water levels. Maps of the hot springs region each cover 0.94 km² and were digitized at 1:300-
351 scale using the highest-resolution data available each year.

352

353 3.3. Hydrological analysis

354 The discharge rate and heat flux of the different streams was investigated in 2016,
355 2017, and 2018 using systematic stream flow measurements, such as flow velocity,
356 temperature, pH, and cross-sectional area. In 2016, temperature and velocity data were taken
357 on different days and at different places as the transects. We therefore used the nearest
358 velocity and temperature measurement within the same stream for each transect. In 2017 and
359 2018, stream transects, velocity, pH, and temperature data were all taken at the same time. For
360 further details, see Appendix B.

361 The discharge rate Q [m³/s] is calculated for each cross-section as follows:

$$362 \quad Q = v \times A, \quad (1)$$

363 where v is the flow velocity [m/s], and A is the cross-sectional area [m²]. Heat flux is then
364 calculated according to:

$$365 \quad E_{flux} = C_p \times \rho \times T \times Q, \quad (2)$$

366 where E_{flux} is the total energy flux [J/s], C_p is the specific heat of water [J/kg/K] at the water
367 temperature, assuming $\rho = 1$ kg/m³ is the water density, and T is the water temperature (K).

368 The hydrology observations are given for each stream in Table B2-4 (Appendix B),
369 summarized in Table 1, and discussed in Section 4.1.

370 To estimate the flow velocity during the July 21, 2016 dam-breaching event, we used
371 Manning's equation:

$$372 \quad v = \frac{R^{2/3} \times \theta^{1/2}}{n}, \quad (3)$$

373 where R is the hydraulic radius [m], θ is the slope at the bottom of the stream [dimensionless],
 374 and n is the Manning coefficient [$\text{s/m}^{1/3}$]. To estimate Manning's n , we used the guide by
 375 Arcement and Schneider (1989), which is primarily based on grain size in the channel, with
 376 adjustments taking into account the vegetation (absent in our case), obstructions, and channel
 377 shape. We find $n = 0.032$, which is close to the value of 0.035 found within the Jökulsá á
 378 Fjöllum river bed by Howard et al. (2012). Under uniform flow conditions, the slope θ at the
 379 bottom of the stream is equal to the slope of the water surface. The hydraulic radius is the
 380 ratio between the cross-sectional area and the wetted perimeter. For an ideal rectangular
 381 channel, it can be calculated as follows:

$$382 \quad R = \frac{W \times D}{W + 2D}, \quad (4)$$

383 where W is the width [m], and D the depth of the channel [m]. The hydraulic radius, and
 384 especially the depth, is the largest source of error in our calculation. Indeed, due to its location
 385 on the far side of the lava flow field, this channel is difficult to access, and a cross-section was
 386 not obtained. Instead, for every meter along the new Jökulsá á Fjöllum riverbed, we extracted
 387 topography profiles from the 2003 DTM from Loftmyndir ehf., the 2015 Lidar data from
 388 NERC, and the 2016 DTM from the Trimble UX5-HP sUAS. For each profile we carried out
 389 measurements of the width and elevation (H_{river}) of the river in 2016, the maximum width and
 390 flood height (H_{flood}) reached by the flood as shown by high water marks (deposited or eroded
 391 material), and the pre-existing width and lowest elevation (H_{2015}) of the depression in 2015.
 392 The widths and depths we measure for the flood depend on whether the flood was eroding,
 393 depositing sediment, or running through an existing channel. The depths of the flood are
 394 calculated as $D = H_{flood} - H_{2015}$ if the flood ran through a pre-existing channel, or as $D = H_{flood}$
 395 $- H_{river}$ if the flood eroded an entirely new stream. However, during the breach, the
 396 morphology of the channel varied very quickly as the channel was excavated and sediment

397 was deposited. This method therefore leads to large uncertainties in the channel depth and in
398 the final discharge rates calculated. The results of these calculations are presented in Section
399 4.3.2.

400

401 **3.4. Climate data**

402 We also examined weather patterns between 2000 and 2018 to determine whether
403 abnormal precipitation or temperature occurred in the Dyngjusandur region in this period.
404 Given the remote location of the region, the closest weather station with publicly available
405 data for this period is located 50 km to the north, and is not representative of the weather at
406 Dyngjusandur. Instead, we use the climate reanalysis data available through the European
407 Centre for Medium-Range Weather Forecasts (ECMWF) ReAnalysis-Interim (ERA-Interim)
408 record. This worldwide dataset combines model predictions with both nearby surface and
409 satellite observations, and gives the resulting data for every 0.125° in latitude and longitude
410 (Dee et al., 2011). We use the monthly precipitation accumulation, and the monthly mean of
411 the daily mean temperature, modeled for the location of the 2014–2015 Holuhraun lava flow
412 (64.875°N, 16.500°W). These data are not direct observations obtained at the site on or near
413 the lava flow field, but are the results of a climate model and the nearest measurements, as
414 given by the ERA-Interim dataset. Although we are using the ERA-Interim dataset as a proxy
415 for weather at the Holuhraun lava flow field, it may include inaccuracies due to both
416 insufficient resolution and lack of ground observations.

417

418 **4. Results**

419 **4.1. Yearly changes in the hot springs region**

420 **4.1.1. Morphological changes**

421 We studied the hydrology of the hot springs region for 2003, 2015, 2016, 2017, and
422 2018. Fig. 7 provide visual context for some key features of this region. Here, water from
423 three different sources meets: clear, cold spring water from seepage channels (Figs. 7c), blue–
424 green water warmed by the lava (Fig. 7b), and milky white glacial meltwater (Fig. 7f). This
425 mixing is particularly evident in one large stream, which remains split in two after the
426 different streams have merged (Fig. 7f). The hot springs and hot pools, which appeared during
427 the eruption, are still present in 2018. In 2015, an important stream of the Jökulsá á Fjöllum
428 approached the lava but entered an eastward-flowing drainage before continuing its flow to
429 the northeast, thereby avoiding the hot springs region (Figs. 6b and 7a). In 2016, water from
430 the eastern lava-dammed lake reached this stream of the Jökulsá á Fjöllum drainage system,
431 and the large water influx was sufficient to break into the hot springs (Figs. 6c, 7d, and 7e).
432 The dam breaching event, which is further discussed in Section 4.3, brought glacial water into
433 the hot springs in 2016, cooling them down and reorganizing them (Fig. 6c). The further
434 modification of the channel morphology from 2016 to 2018 is mostly due to daily changes in
435 water level. Even though in 2018 there is more glacial water and more seepage activity than in
436 2017, the morphology of the streams remains the same, indicating that the system has reached
437 a more stable layout. The hydrological system on Dyngjusandur is thus gradually stabilizing
438 after the large disruption by the new lava.

439 Before the eruption, there was already some seepage activity very close to the main
440 bed of the Jökulsá á Fjöllum, which forms a topographic low within the sandsheet (Fig. 6a).
441 Over the summers following the eruption, we observed the development of seepage channels
442 around the hot springs, in particular to the north of the lava, which is covered by a much older
443 basaltic lava flow (Fig. 6b–e; closer views in Figs. 7c and 7f). Indeed, the area of surface
444 water north of the riverbed of Jökulsá á Fjöllum (see Fig. 6) increased in size from 2,500 m²
445 in 2003, to 38,100 m² in 2015, to 53,200 m² in 2016, decreased to 26,900 m² in 2017, and

446 grew back to 38,300 m² in 2018 (Table 1). Although there are some hot springs in this area, it
447 is largely dominated by seepage channels, and the yearly changes in this area thus reflect
448 shifting water tables. Seepage activity at Svartá seems to match the patterns observed in the
449 hot springs region: it was high in 2016 and 2018, and lower in 2017. Given that the source of
450 Svartá is located 2 km north of the hot springs and has an elevation that is approximately 3 m
451 higher than the seepage channels in the hot springs region, these observations imply that
452 seepage at Svartá and the hot springs region originates from the same shallow aquifer. The
453 water table in this shallow aquifer rose in 2015, and was considerably higher in 2016 and
454 2018 than in 2015 and 2017.

455 In the summer of 2017, dozens of small artesian fountains were observed near the hot
456 springs region, near profiles #9, #7, and #17 in Fig. 8b. Water associated with the artesian
457 fountains bubbled out of the ground with heights typically less than 10 cm. Their fountains
458 were generally a few centimeters wide and clustered near the heads of some seepage channels.
459 They were only observed on a sunny day after a stretch of colder and overcast weather, and
460 were thus correlated with a sudden rise in the water level due to increased glacial melt. It is
461 likely that the shallow aquifer feeding the seepage channels is partly confined by the ancient
462 lava. Thus there is a lag between the rise in water table and the rise in water level in the
463 seepage channel. This lag is sufficient to create a small artesian head, pushing the water up
464 tens of cm. This explains why no artesian springs were observed in 2016 or 2018 in spite of
465 higher water levels.

466

467 **4.1.2. Hot springs characteristics**

468 The water entering the hot lava either exits down-flow to form hot springs, or it
469 vaporizes into steam en route to form fumeroles. Due to the cooling of the lava, most
470 fumeroles were gone by 2016, though in 2016 and 2018 levels of fumerolic activity were

471 observed to increase on warm days when there were higher volumes of glacial runoff. We
472 attribute enhanced fumarolic activity on warmer days to the water table reaching the level of
473 residual heat sources within the core of the lava flow field, thus generating steam. In 2017,
474 when water levels in the region were lower, no major fumaroles were observed.

475 The water that emerged from the lava along with several nearby glacial and seepage
476 streams were examined during the summers of 2016, 2017, and 2018 and the results are
477 shown in Fig. 8. For each cross-section, we calculated discharge rate and heat flux through
478 each stream (see Appendix B). These values only represent a snapshot in time for a very
479 dynamic system: the water levels varied throughout the day and from day to day, leading to
480 changes in discharge and heat flux. Estimates of the total discharge rate and total heat flux
481 from the heated water going through the lava were then made by combining information from
482 multiple stream segments, while excluding glacial water contribution (profile #7 in 2016,
483 profile #28 in 2017, and profile #1 in 2018); they are given in Table 1.

484 While they do not fully illustrate the high-frequency variations over time, the 2016–
485 2018 field observations allow us to quantify general trends in the annual distribution of
486 temperatures, discharge rates, and heat fluxes in the hot springs region. For example, in the
487 summer of 2016, all hot spring temperatures had decreased to below 20°C (Fig. 8). Yet, even
488 in 2016 Vatnajökull National Park rangers recorded high water temperatures in pools within
489 the lava (Sigurður (Siggi) Erlingsson, personal communication, 2017), reaching up to 41 °C in
490 the late summer (i.e., August to mid-September) of 2016. The hottest temperatures
491 corresponded to dates when the water reached a maximum depth of 1.8 m within the pool. By
492 late September, the water level decreased to 1.4 m within the pool and the temperature
493 correspondingly decreased to 33 °C. This implies that in 2016, the lava contained significant
494 residual thermal energy that was available to heat water, but only if the water table rose high
495 enough for the water to be warmed by the hot interior of the flow. In 2017, water depths in the

496 pool were considerably lower—just 20–30 cm at the same locality—and maximum
497 temperatures were about 10°C. The changing morphology of the river, caused by the dam
498 breaching event and migration of streams, can result in varying water levels and mixtures of
499 water of different origins. For instance, the discharge rate through the hot springs (Table 1) in
500 2016 is more than twice as high as in 2017 and 2018, which may be explained either by
501 residual water from the recent dam-breaching event (a week earlier) or by extra glacial water
502 entering the hot springs.

503 Changes in stream temperature and discharge rate from year to year are thus explained
504 by three interacting processes: gradual cooling the lava flow core, changing configurations of
505 lava-dammed lakes and stream locations, and changing water table levels.

506

507 **4.1.3. Annual weather patterns**

508 To determine whether the observed changes in water table and discharge rates were
509 linked to the 2014–2015 Holuhraun eruption and/or to weather patterns, we examined the
510 modeled total precipitation and mean daily temperature data described in Section 3.4, for the
511 Holuhraun area. These datasets are shown in Tables 1 and 2 for the summers of 2003 and
512 2013–2018. Section 4.1.1. discussed how the groundwater level at Svartá and at the distal end
513 of the 2014–2015 Holuhraun lava flow field rose considerably after the eruption, and has not
514 dropped back to its original level. Temperature and precipitation patterns within the
515 Holuhraun region do not appear sufficiently different during the 2015–2018 time period to
516 fully explain such a large and lasting change (Tables 2 and 3). Consequently, the local rise in
517 groundwater level and seepage channel activity was probably affected to some degree by the
518 lava itself.

519 Weather patterns might however explain year-to-year changes in groundwater level.
520 Indeed, we have seen in Section 4.1.1. that the groundwater levels were higher in 2016 and

521 2018 compared to 2015 and 2017 (though all were higher than before the eruption). A one-to-
522 one correlation between groundwater level and either precipitation or temperature is not
523 observed, because variations in water table are a consequence of a variety of factors. Annual
524 differences may be due to differences in the volumes of snow and ice that accumulated each
525 year prior to melting (especially on Askja and Vaðalda), possible dust storms or volcanic
526 eruptions depositing ash or dust on the glacier, and atmospheric conditions over the summer
527 months (e.g., temperature, cloud cover/insolation, humidity, precipitation, wind, etc.). Finally,
528 changes in glacial stream organization may also have a profound effect by altering the
529 proportion of available water being transported by fluvial versus groundwater systems.

530

531 **4.2. Effects of continuous processes**

532 Continuous processes causing hydrological changes around the Holuhraun lava field
533 appear to be related to two interlinked causes: daily variations in meltwater
534 discharge/generation from the glacier, and the subtle changes in the level of the groundwater
535 table at Svartá and at the distal end of the 2014–2015 Holuhraun lava flow field over longer
536 periods of time. Among the annual changes described in Section 4.1.1, the expansion of
537 seepage channels, the variations in glacial melt contribution, and the small reorganization of
538 the channel morphologies are caused by continuously acting agents of change.

539 During the 2016 field campaign, we obtained high-resolution sUAS images of the
540 same area on two different days and at two different times of the day, allowing us to observe
541 small, continuous changes in action. The 1 cm/pixel imagery over the hot springs region was
542 taken on July 28, and the 4 cm/pixel imagery was taken on July 30–31. Four different types of
543 changes were observed: modifications in the braided stream morphology (Fig. 9a), channel
544 bank erosion (Fig. 9b), different water levels in the incoming glacial river (Fig. 9c), and
545 finally a single instance of seepage channel headward expansion (Fig. 9d). The difference in

546 water level (Fig. 9c) observed in the newly dug glacial stream is due to the time at which the
547 orthoimagery was taken in that area: around 10:30 AM on July 28 and around 6:00 PM on
548 July 30, 2016. During the summer, the water level in the Jökulsá á Fjöllum river increases as
549 the day progresses and the ice melted by the incoming solar radiation travels from the
550 Vatnajökull glacier to the region of interest.

551 Morphological changes (Fig. 9a), including channel bank erosion (Fig. 9b), are
552 expected within braided streams, especially during periods of high discharge (Goff and
553 Ashmore, 1994). Indeed, the lack of vegetation, regular removal of fines in suspension within
554 the flow, and the frequent fluctuations in water level make proglacial braided streams
555 particularly unstable (Maizels, 2002). An added factor of instability at the time of our
556 observations is the recent dam-bursting event, which occurred a week earlier, on July 21–22,
557 2016 (Sigurður (Siggi) Erlingsson, personal communication, 2016). This event drastically
558 modified the local braided stream morphology, with the system continuing to seek a new
559 equilibrium.

560 The seepage channel expansion observed between July 28 and July 30, 2016 (Fig. 9d)
561 is caused by groundwater sapping. This process may have been enhanced by a local rise in the
562 groundwater table following the dam-breaching event approximately one week before, which
563 supplied more water to the area. Similarly, the new seepage activity seen in 2015 and 2016 to
564 the north of the lava flow is also the result of groundwater sapping progressively eroding the
565 riverbank.

566

567 **4.3. Effects of catastrophic processes**

568 **4.3.1. Dam-breaching event: chronology**

569 The eastern lava-dammed lake (Fig. 3c) was formed by glacial streams, which used to
570 feed the Jökulsá á Fjöllum and became dammed by the 2014–2015 Holuhraun lava flow field.

571 It was located approximately 4 km to the southwest of the hot springs. On September 8, 2015,
572 it covered an area of approximately 0.25 km², but its water level varied daily. This lake was
573 essentially stable in its location until July 2016. The sequence of events leading to glacial
574 water pouring into the hot springs is described below and is illustrated for a small part of the
575 lava flow margin in Fig. 10, and for a larger region in Fig. 11.

576 In 2015, the water that had accumulated over the summer caused a minor outflow,
577 entrenching a small channel along the edge of the lava flow (Fig. 10c). However, water from
578 this event never reached the main channel in the hot springs region, but instead percolated
579 into the ground and the lava, allowing the lake to retain its overall stability. Water continued
580 to accumulate in the dammed lake in summer of 2016, until it breached into the hot springs in
581 July 2016. Timing of the 2016 dam-breaching event, described here, was constrained by the
582 eyewitness account of rangers within the Vatnajökull National Park (Bonney et al., 2017).
583 On July 15, 2016, a small trickle of water developed along the southeastern side of the flow.
584 This glacial water from the lake met with another glacial stream (Fig. 11, Location 3).
585 Together they breached into the hot springs on July 21 by creating a relatively small gap
586 through the old riverbank (Fig. 11, Location 4; also visible in Fig. 6c). The main phase of the
587 breach occurred on July 22, when glacial water began flowing into the hot springs with large
588 waves pouring through this gap next to the lava. On July 22 and 23, a huge steam plume was
589 seen rising from the location of the former lake, probably caused by large amounts of water
590 flowing into new, still-hot regions of the lava. After the breach, water primarily flowed along
591 the edge of the lava, but observations of water flowing through pools in the lava and from the
592 springs located at the distal flow margin imply that some water continued to flow through and
593 beneath the lava. After July 22, glacial stream water and water from the hot springs merged to
594 produce braided network streams with a wide range of temperatures.

595

596 **4.3.2. Dam-breaching event: magnitude and consequences**

597 The new stream eroded by the dam-breaching event of July 22, 2016 is 20–70 m wide
598 and 2 km long. Fig. 11 shows that a depth of at least 5 m of sediment was carried away as it
599 excavated the new channel. The channel was modified during and after the dam breaching
600 event, for example by stream bank erosion and sediment deposition: the maximum erosion
601 depths during the breach are therefore unknown. Furthermore, significant amounts of
602 sediment were deposited on top of the lava (Fig. 11), which in places was topographically
603 lower than the surface of the adjacent sandsheet. Exact sediment volume deposited on the lava
604 cannot be calculated as the river now flows on top of the lava in several places.

605 Flow velocity and discharge rate vary with the width and depth of the channel.
606 Locations of sedimentation (e.g., profiles A to A' and C to C' in Fig. 12) cannot be used to
607 estimate the original depth and width of the flood: the water velocity was lower in these
608 places and entrained sediment was deposited, changing the morphology of the channel during
609 the flood. Profiles where either the flood ran through an existing channel shape (e.g., profile B
610 to B' in Fig. 12) or entrenched an entirely new channel (e.g., profile D to D' in Fig. 12) are
611 used to estimate the width and depth of the channel for water velocity and discharge rate
612 calculations. Using these profiles and assuming the channel was brim full, we estimate a flow
613 velocity of 6.2 ± 0.3 m/s, giving a discharge of $1,200 \pm 250$ m³/s just downstream of the
614 breach. This discharge is two to three orders of magnitude larger than the total discharge from
615 the hot springs (2.2–14.0 m³/s, Table 1), explaining how effective the dam-breaching event
616 was for both erosion and sediment transport.

617 Sediment deposition on top of the lava and redirection of the river in 2016 caused a
618 retreat of the visible lava margin compared to that of 2015. There are two regions where we
619 have imagery of ≤ 4 cm/pixel in the summers of both 2015 and 2016: the hot springs region
620 (Fig. 6) and the dam-breaching region (Fig. 11). Comparing the lava margin in 2015 and 2016

621 shows that 7,421 m² of lava have been covered by sand and/or water. In contrast, the northern
622 margin of the lava, which is not in contact with an active branch of the Jökulsá á Fjöllum,
623 shows no such retreat of the visible lava flow margin.

624

625 **5. Discussion**

626 **5.1. Origin of the hot springs**

627 After the end of the Holuhraun eruption in February 2015, glacial meltwater ponded at
628 the entry points into the lava, causing the formation of two lakes banked against the lava flow:
629 one in the west, and the other in the east—relatively close to the hot springs region (Fig. 3).

630 The lava is the main outlet for these lakes, and it is likely that most of the warm water
631 forming the hot springs came from these lakes after taking different paths through the lava.

632 After the eastern lake drained into the hot springs region in 2016, its contribution to water flux
633 through the lava has greatly decreased, leaving the western lake as the main source of heated
634 water for the hot springs. Given that the western lake is further from the hot springs than the
635 eastern lake (12.1 km vs 2.8 km), the hot springs take more time to respond to changes in the
636 western lake. Thus, even though the lake is primarily controlled by glacial melt, the flux at the
637 hot springs is not expected to be directly correlated to the time of day or to weather
638 conditions. Additionally, as the lava flow cooled from above and below, residual heat
639 concentrated within the core of the flow and was only able to warm the water when the depth
640 of the water table approached the portions of the flow that were still hot. Consequently, when
641 the eastern lava-dammed lake failed and drained in late July 2016, the water table would have
642 locally lowered, thereby reducing the temperature of the water emerging from the hot springs
643 until the groundwater table gradually increased in late August to early September.

644

645 **5.2. Origin of the seepage channels**

646 The development of seepage channels shown in Fig. 6 can be explained with several
647 interacting processes responsible for the reorganization of the groundwater flow: changes in
648 the level of the water table, a reorganizing of the groundwater flow, development of artesian
649 springs, escape of lava-heated water, and/or the formation of a layer of reduced permeability
650 under and around the lava. In all cases, the springs that form will have the morphology of
651 seepage channels, because the surface consists of unconsolidated sediment. Some of the
652 groundwater emerging at the seepage channels probably percolates into the lava, but since the
653 lava is already saturated with water, most of it forms small streams flowing along the margin
654 of the lava towards the hot springs (Fig. 13b).

655 Variations in seepage activity in 2015–2018 affecting simultaneously Svartá (Fig. 4)
656 and seepage channels near the hot springs (Fig. 6) suggest variations in the water table at
657 distances of up to 2 km from the lava flow field. As detailed in section 4.1.3., the baseline
658 groundwater level may be responding to annual differences in glacial melt from Vatnajökull
659 as well as snowmelt from more local sources such as the Askja massif and Vaðalda. Thus,
660 weather patterns may explain yearly changes (higher groundwater levels in 2016 and 2018),
661 but they are insufficient to account for the long-lasting rise in water table after the eruption. A
662 possibility we considered is a pulse of glacial melt from the eruption slowly moving through
663 the groundwater system, which is supported by the presence of ice cauldrons indicating
664 subglacial eruptions (Reynolds et al., 2017). However, the water level would then be expected
665 to fall back after the meltwater travels through the groundwater system. Furthermore,
666 Reynolds et al. (2017) estimate that only about 23 million m³ of ice melted during these
667 subglacial eruptions. For comparison, this corresponds to five days of winter flux of the
668 Jökulsá á Fjöllum through Upptyppingar (discharge rate of 55–60 m³/s, Gylfadóttir, 2016),
669 and it would thus contribute little to the aquifer.

670 Our preferred interpretation of the surface and groundwater flow before and after the
671 2014–2015 eruption is illustrated schematically in Fig. 13. It is likely that both before and
672 after the eruption there is an aquifer carrying groundwater from the area of the Dyngjujökull
673 glacier towards the northeast, flowing below the old bed of the Jökulsá á Fjöllum and the
674 2014–2015 Holuhraun lava flow (Baldurson et al., 2018). Lake Dyngjuvatn, the western lava-
675 dammed lake, and snowmelt from Askja and Vaðalda may all contribute either to this aquifer,
676 or to a shallower groundwater system, though it is impossible to identify the dominant source
677 of water feeding Svartá and the hot springs without a dedicated study. Nonetheless, springs
678 were known to exist within the bed of the Jökulsá á Fjöllum, supplying about 20 m³/s to the
679 river (Baldurson et al., 2018; Esther Hlíðar Jensen, personal communication, 2018). The area
680 where this groundwater emerged is now covered in lava preventing the groundwater from
681 entering the old riverbed (Fig. 13b). The portion of the water that would otherwise occupy the
682 former river channel is then displaced into the adjacent groundwater system, raising the water
683 table.

684 The emplacement of lava into the riverbed also had subtler effects on the groundwater
685 flow. Indeed, a slight rise in the water table around the lava focused water into the
686 topographic low formed between the pre-eruption topography and the lava creating a new
687 small channel running parallel to the northern lava flow margin (Fig. 13b). The lava-dammed
688 lakes also probably have an important role in the local water table. We infer from our
689 observations that the water entering the groundwater system from the western lake both flows
690 through the lava flow and spreads out along the left bank of the former river channel to supply
691 water into the adjacent part of the sandsheet. This additional groundwater supply in and near
692 the lava may have contributed to the elevated level of seepage channel activity observed near
693 the lava. This hypothesis is supported by eyewitness observations by the authors and local
694 park rangers, which suggest a correlation between high water levels in the western lava-

695 dammed lake and increased seepage activity about a day later. However, the phase lag
696 introduced by surface runoff entering into the groundwater system through the lava-dammed
697 lake complicates straightforward correlations. It is thus unclear how far from the lava the
698 water from the western lava-dammed lake can affect the groundwater system, and whether or
699 not it could have affected Svartá.

700 Galeczka et al. (2016) documented an increase in activity of cold-water springs near
701 the lava front after the eruption, and attributed it to an increase in the subsurface water
702 pressure under the weight of the lava flow. However, we only observed artesian fountaining
703 during the warmest days of August 2017, probably caused by a rapid rise in the water table
704 (Section 4.1.1). This implies that short-term changes in the supply of glacial melt water also
705 have an impact on the development of transient artesian fountains. An artesian system, with
706 the aquifer being constrained either by the 2014–2015 lava or by much older lava, likely plays
707 a role in the seepage channel expansion, but cannot explain the changes in activity 2 km away
708 at Svartá.

709 Hydrothermal precipitates (e.g., carbonates, sulfates, and/or silicates) may have filled
710 the pore spaces in the subsurface, thereby reducing the permeability of the surrounding
711 substrate and modifying groundwater flow (Fig. 13). The water going through the lava, aided
712 by the high temperatures within, dissolved the components of the basalt and as these
713 hydrothermal fluids entered the substrate and formed precipitates. Indeed, Galeczka et al.
714 (2016) found the water samples at the lava front to be supersaturated with respect to Al-
715 bearing secondary phases including gibbsite, imogolite, kaolinite, and Ca-montmorillonite. If
716 this supersaturated water entered the sandy/gravelly groundwater system and cooled down,
717 these secondary phases could precipitate out of the water, filling the pore spaces. The layer of
718 reduced porosity could then affect the path of subsurface water flow and contribute to the
719 formation of seepage channels. Such a layer could reduce the exchange of groundwater going

720 through the lava with that going under and around the lava. However, a low-permeability
721 layer alone could not cause the observed changes in water level, so we do not consider it to be
722 a dominant driver of hydrological change in this region.

723 It is likely that a rise in the water table represents the primary cause of increased
724 seepage channel activity near the lava flow margin in 2015–2016. However, small artesian
725 springs and changes in the permeability of the substrate beneath the lava by hydrothermal
726 precipitation may have accelerated the formation of seepage channels. Indeed, an artesian
727 pressure system would be particularly effective in enhancing seepage erosion at times when
728 the groundwater table is higher, and a low permeability layer beneath the lava could reduce
729 the flow of water into the former river channel bed, thereby directing flow toward the surface
730 in regions adjacent to the lava. These mechanisms may therefore have contributed to feedback
731 mechanisms that enhanced seepage erosion.

732

733 **5.3. Continuous versus catastrophic processes**

734 Although most geologic work is done by large, catastrophic events rather than low-
735 amplitude, continuous processes, the relative contributions of catastrophic versus incremental
736 or continuous processes remain debated (Melosh, 2011). The Holuhraun 2014–2015 eruption
737 initiated both catastrophic and continuous processes of landscape evolution.

738 The largest hydrological changes in the region, including erosion and sediment
739 deposition of up to 5 m, were brought about by the 2016 dam-breaching event, as a new
740 riverbed was entrenched along the margin of the lava flow (Section 4.3). The discharge rate
741 during the breach was over two orders of magnitude larger than the normal discharge rate in
742 the hot springs in the same year, but was concentrated to a channel only tens of meters across.
743 The large area of lava covered by sediment is especially significant as it illustrates the first

744 major step in the degradation of a lava flow. The dam-breaching event also modified the
745 morphology and the temperature distribution in the hot springs region (Section 4.1).

746 Continuous processes, however, have also caused appreciable change in the region
747 over only three years. The first snowmelt after the end of the eruption may have had the
748 largest contribution to the partial burial of lava flow margins, which appear to have already
749 been mantled in sediment by the time the first aerial images were acquired in August 24,
750 2015. Subsequent snow melts, rainfall, and aeolian sediment transport do not appear to have
751 had significant erosional or depositional effects in the region of interest over our timescale of
752 observation. The continuous movements of the braided stream, due mainly to daily changes in
753 glacial melt, cause a regular redistribution of the channels and terraces, though these changes
754 have low preservation potential. Daily and yearly changes in groundwater flow have
755 contributed to the development of new seepage channels in the hot springs region through
756 headward erosion and the redistribution of sediments. While having very low discharge, the
757 area covered by active seepage channels increased by a factor of fifteen over the first eighteen
758 months following the end of the eruption, although the topography difference is mostly below
759 the resolution of the DTMs. Although groundwater seepage decreased in 2017, the
760 topography created by this process during the two previous years remains, indicating that the
761 change in the landscape may be long-lasting.

762 Contributions to landscape evolution of catastrophic and continuous processes are
763 therefore very different, but both appear to be important to our understanding of the
764 hydrology in the region.

765

766 **5.4. Implications for Mars**

767 Groundwater seepage, weakening bedrock through chemical and physical weathering
768 processes, may also have formed theater-headed valleys on Mars (Baker et al., 1990, 2015;

769 Goldspiel and Squyres, 2000; Gulick, 2001; Harrison and Grimm, 2005; Mangold et al.,
770 2008), though other processes may also be able to form similar morphologies (Howard et al.,
771 2005; Lamb et al., 2006; Luo and Howard, 2008). While the groundwater seepage
772 interpretation remains under debate for large theater-headed valleys such as Nirgal Vallis or
773 parts of Vallis Marineris (Lamb et al., 2006; Luo and Howard, 2008; Mangold et al., 2008;
774 Pelletier and Baker, 2011; Marra et al., 2015), it is possible that groundwater seepage played a
775 role in the formation of smaller channels in cohesionless sediments during Mars' early, wet
776 history, though these channels would have been largely eroded by now (Craddock and
777 Howard, 2002; Luo and Howard, 2008). Recently, Pendleton (2015) and Nahm et al. (2016)
778 invoked groundwater seepage to explain very young theater-headed channels in the source
779 region of the Athabasca Valles flood lava flow. These features, also described by Balme and
780 Gallagher (2009), are morphologically similar to seepage channels on Earth such as the ones
781 by the Holuhraun lava flow field, but are difficult to reconcile with their occurrence in a
782 geologically young (<20 Ma) lava-mantled Martian setting (Bermann and Hartmann, 2002;
783 Jaeger et al., 2010). Our direct observations of the changes wrought upon groundwater
784 seepage by a lava flow at Holuhraun may serve as a useful analog to shed light upon Martian
785 seepage channels.

786 The Dyngjussandur region provides an excellent analog for Mars (Hamilton, 2015;
787 Richardson et al., 2018), and even before the 2014–2015 eruption, it has been compared to
788 sandsheets on Mars (Baratoux et al., 2011). These similarities stem from the high altitude, low
789 temperature, prevalence of basaltic sand, and almost complete lack of vegetation at
790 Dyngjussandur. Though much smaller, the 2014–2015 Holuhraun lava flow field is also a good
791 analog for Martian flood lava flows (Voigt et al., 2017), such as the recent (<20 Ma) low-
792 viscosity basaltic flood lavas having erupted from the Cerberus Fossae in Athabasca Valles,
793 Rahway Valles, Marte Vallis, or Amazonis Planitia (Lanagan et al., 2001; Fuller and Head,

794 2002; Voigt and Hamilton, 2018). Future studies would therefore benefit from using the
795 Holuhraun seepage channels as an analog to morphologically similar landforms in volcanic
796 settings on Mars.

797

798 **6. Conclusions**

799 The emplacement of the 2014–2015 Holuhraun lava flow field modified the landscape
800 and affected the local hydrology in a variety of ways. The lava was emplaced onto part of the
801 Jökulsá á Fjöllum river’s flood plain, infilling former stream channels and affecting the path
802 of glacial melt water. Where active stream channels were blocked by the flow margin, lava-
803 dammed lakes formed. The water level within these lakes varied on a diurnal basis during the
804 summer months, changing in response to rates of glacial melting. Much of the lake water
805 percolated into the lava, cooling the lava flow and emerging from the flow front as hot
806 springs. However, in 2016 the capacity of the lava-dammed lake located along the eastern
807 margin of the flow was exceeded, which triggered overland water flow and ultimately a dam-
808 breaching event on July 22, 2016. This flood caused sudden changes within the hydrological
809 system and in erosion and sediment depositional rates. In addition to this catastrophic event as
810 an agent of change, there were also continuous hydrological processes in the region that
811 caused changes in the landscape. Cold seepage springs developed next to the lava flow margin
812 and the level of water changed yearly within the existing seepage channel, Svartá, which is
813 located 2 km away from the lava flow front. Temperature and precipitation records indicate
814 that 2015–2018 was not an atypical period in terms of the decadal-scale weather patterns in
815 the region, which suggests that the observed hydrological changes were caused by the
816 emplacement of the 2014–2015 Holuhraun lava flow field. We also conclude that the
817 formation of lava-dammed lakes and the infiltration of water into the lava and surrounding
818 substrate affected seepage channel activity, water-enhanced lava cooling rates, and hot springs

819 temperatures. Following the collapse of the eastern lava-dammed lake, the western lake likely
820 provides the dominant control over local hydrological processes. Therefore, monitoring
821 hydrological and landscape evolution processes associated with the 2014–2015 Holuhraun
822 lava flow field provides a rare opportunity to document how environments respond to large
823 basaltic lava eruptions, and it provides an exceptional ground-truth example crucial for
824 interpreting the geologic record of volcanic landscapes on other planets, particularly on Mars.

825

826 **Acknowledgements.** The authors thank the Vatnajökull National Park Service
827 (Vatnajökulspjóðgarður) for access to the study region, Vatnajökull National park rangers for
828 their help and hospitality at Drekgil, and Park Ranger Sigurður (Siggi) Erlingsson for many
829 informative discussions relating to the changing environmental conditions within the
830 Holuhraun region. We also thank Victor Baker for discussions related to hydrological
831 processes and others who assisted our team in the field. Specifically, we would like to thank
832 Laszlo Keszthelyi and Colin Dundas (2015), Joana Voigt and Kristina Lincoln (2016),
833 Muhammad AUFARISTAMA and Alma Gytha Huntington-Williams (2017), and Sarah Sutton and
834 Jennifer Eigenbrode (2018). The IsViews project (Iceland subglacial Volcanoes
835 interdisciplinary early warning system), funded by the Bavarian State Ministry of Economic
836 Affairs and Media, Energy and Technology (ID 20-8-34102-15-2012), is gratefully
837 acknowledged, as well as the German company GeoFly acquiring and processing the airborne
838 UltraCam-Xp data for IsViews. Agúst Gudmundsson, Fjarkönnun ehf. is gratefully
839 acknowledged for his support with the organization and management of UltraCam-Xp camera
840 flights. We also thank the Icelandic research center (Rannsóknamiðstöð Íslands) for granting
841 fieldwork permits (2014–2018) as well as the director of the Vatnajökulspjóðgarður, Þórdur
842 H. Ólafsson for the special permit at Holuhraun. Finally, the authors thank Ingrid Utskins as
843 well as two anonymous reviewers for their detailed and helpful reviews, which led to

844 significant improvement of this paper. Funding support was provided by NASA Planetary
845 Geology and Geophysics Grant # NNX14AL54G, and the University of Arizona's Carson
846 Fellowship program.

847

848 **7. References**

849 Alho, P., Russell, A.J., Carrivick, J.L., Käyhkö, J., 2005. Reconstruction of the largest

850 Holocene jökulhlaup within Jökulsá á Fjöllum, NE Iceland. *Quaternary Science*

851 *Reviews*, 24(22), 2319–2334. <http://dx.doi.org/10.1016/j.quascirev.2004.11.021>

852 Allen, M.B., Mark, D.F., Kheirkhah, M., Barfod, D., Emami, M.H., Saville, C., 2011.

853 $^{40}\text{Ar}/^{39}\text{Ar}$ dating of Quaternary lavas in northwest Iran: constraints on the landscape

854 evolution and incision rates of the Turkish-Iranian plateau. *Geophysical Journal*

855 *International*, 185(3), 1175–1188. <http://dx.doi.org/10.1111/j.1365->

856 [246X.2011.05022.x](http://dx.doi.org/10.1111/j.1365-246X.2011.05022.x)

857 Arcement, G.J., Schneider, V.R., 1989. Guide for selecting Manning's roughness coefficients

858 for natural channels and flood plains. *United States Geological Survey Water-Supply*

859 *Paper*, 2339, 1–38. <http://pubs.er.usgs.gov/publication/wsp2339>

860 Arnalds, O., Dagsson-Waldhauserova, P., Olafsson, H., 2016. The Icelandic volcanic aeolian

861 environment: Processes and impacts—A review. *Aeolian Research*, 20, 176–195.

862 <http://dx.doi.org/10.1016/j.aeolia.2016.01.004>

863 AUFARISTAMA, M., HOSKULDSSON, A., ULFARSSON, M.O., JONSDOTTIR, I., THORDARSON, T., 2019. The

864 2014–2015 lava flow field at Holuhraun, Iceland: using airborne hyperspectral remote

865 sensing for discriminating the lava surface. *Remote Sens.*, 11(5), 476,

866 <http://doi.org/10.3390/rs11050476>

867 Bahr, Th., 1997. Hydrogeologische Untersuchungen im Skeidarársandur (Südisland). Diss.,

868 Münchner Geol. Hefte, B 3. Seiten 142-3.

869 Baker, V.R., Kochel, R.C., Laity, J.E. and Howard, A.D., 1990. Spring sapping and valley
870 network development. *Special Paper of the Geological Society of America*, 252, 235-
871 265, <http://dx.doi.org/10.1130/SPE252-p235>

872 Baker, V.R., Hamilton, C.W., Burr, D.M., Gulick, V.C., Komatsu, G., Luo, W., Rice Jr, J.W.,
873 Rodriguez, J.A.P., 2015. Fluvial geomorphology on Earth-like planetary surfaces: A
874 review. *Geomorphology*, 245, 149–182.
875 <http://dx.doi.org/10.1016/j.geomorph.2015.05.002>

876 Baldursson, S, J Guðnason, H Hannesdóttir & T Thórðarson. 2018. Nomination of
877 Vatnajökull National Park for inclusion in the World Heritage List. Reykjavík:
878 Vatnajökull National Park.

879 Balme, M.R., Gallagher, C., 2009. An equatorial periglacial landscape on Mars. *Earth and*
880 *Planetary Science Letters*, 285(1–2), 1–15.
881 <http://dx.doi.org/10.1016/j.epsl.2009.05.031>

882 Baratoux, D., Mangold, N., Arnalds, O., Bardintzeff, J.M., Platevoet, B., Grégoire, M., Pinet,
883 P., 2011. Volcanic sands of Iceland-Diverse origins of aeolian sand deposits revealed
884 at Dyngjúsandur and Lambahraun. *Earth Surface Processes and Landforms*, 36(13),
885 1789–1808. <http://dx.doi.org/10.1002/esp.2201>

886 Berman, D.C., Hartmann, W.K., 2002. Recent fluvial, volcanic, and tectonic activity on the
887 Cerberus plains of Mars. *Icarus*, 159(1), 1–17.
888 <http://dx.doi.org/10.1006/icar.2002.6920>

889 Bonnefoy, L.E., Hamilton, C.W., Scheidt, S.P., Voigt, J., Hoskuldsson, À., Jónsdóttir, I.,
890 Thordarson, T., 2017. Landscape Evolution after the 2014–2015 Lava Flow at
891 Holuhraun, Iceland. In *Lunar Planetary Science Conference (Vol. 48)*, Abstract 1652.

892 Bonny, E., Thordarson, T., Wright, R., Höskuldsson, A., Jónsdóttir, I., 2018. The volume of
893 lava erupted during the 2014 to 2015 eruption at Holuhraun, Iceland: a comparison

894 between satellite- and ground-based measurements, *Journal of Geophysical Research:*
895 *Solid Earth*, 123, 5412–5426. <https://doi.org/10.1029/2017JB015008>

896 Cosyn, P., Miller, R. 2013. Trimble UX5 Aerial Imaging Solution – A new standard in
897 accuracy, robustness and performance for photogrammetric aerial mapping. White
898 Paper, Trimble Navigation limited, 7pp. Available online at
899 uas.trimble.com/media/downloads.

900 Cousins, C.R., Crawford, I.A., Carrivick, J.L., Gunn, M., Harris, J., Kee, T.P., Karlsson, M.,
901 Carmody, L., Cockell, C., Herschy, B., Joy, K.H., 2013. Glaciovolcanic hydrothermal
902 environments in Iceland and implications for their detection on Mars. *Journal of*
903 *Volcanology and Geothermal Research*, 256, 61–77.
904 <http://dx.doi.org/10.1016/j.jvolgeores.2013.02.009>

905 Craddock, R.A., Howard, A.D., 2002. The case for rainfall on a warm, wet early
906 Mars. *Journal of Geophysical Research: Planets*, 107(E11).
907 <http://dx.doi.org/10.1029/2001JE001505>

908 Dee, D.P., Uppala, S.M., Simmons, A.J., Berrisford, P., Poli, P., Kobayashi, S., Andrae, U.,
909 Balmaseda, M.A., Balsamo, G., Bauer, D.P., Bechtold, P., 2011. The ERA-Interim
910 reanalysis: Configuration and performance of the data assimilation system. *Quarterly*
911 *Journal of the royal meteorological society*, 137(656), 553–597.
912 <http://dx.doi.org/10.1002/qj.828>

913 Deligne, N.I., 2012. After the flow: Landscape response to the emplacement of Holocene lava
914 flows, central Oregon Cascades, USA [Ph.D. thesis]: Eugene, Oregon, University of
915 Oregon, 217 p.

916 Dirscherl, M., Rossi, C. 2017. Geomorphometric analysis of the 2014–2015 Bárðarbunga
917 volcanic eruption, Iceland. *Remote Sensing of Environment*, 204, 244–259.
918 <http://dx.doi.org/10.1016/j.rse.2017.10.027>

919 Dundas, C.M., Keszthelyi, L., Hamilton, C.W., Bonnefoy, L.E., Scheidt, S.P., Lev, E.,
920 Rumpf, M.E., Thordarson, T., Hoskuldsson, A., Jonsdottir, I., Keske, A.L., 2017. The
921 hydrothermal system of the 2014–2015 lava flows at Holuhraun, Iceland: An analog
922 for Martian lava–water interactions. In *Lunar and Planetary Science Conference* (Vol.
923 48), Abstract 2470.

924 Dunne, T., 1980. Formation and controls of channel networks. *Progress in Physical*
925 *Geography*, 4(2), 211–239. <http://dx.doi.org/10.1177/030913338000400204>

926 Dunne, T., 1990. Hydrology, mechanics, and geomorphic implications of erosion by
927 subsurface flow. In *Groundwater Geomorphology: The Role of Subsurface Water in*
928 *Earth-Surface Processes and Landforms*, 252, 1–28. [https://doi.org/10.1130/SPE252-](https://doi.org/10.1130/SPE252-p1)
929 [p1](https://doi.org/10.1130/SPE252-p1)

930 Eibl, E.P., Bean, C.J., Vogfjörd, K.S., Ying, Y., Lokmer, I., Möllhoff, M., O’Brien, G.S.,
931 Pálsson, F., 2017. Tremor-rich shallow dyke formation followed by silent magma flow
932 at Bárðarbunga in Iceland. *Nature Geoscience*, 10(4), 299–304.
933 <http://dx.doi.org/10.1038/NGEO2906>

934 Ely, L.L., Brossy, C.C., House, P.K., Safran, E.B., O’Connor, J.E., Champion, D.E., Fenton,
935 C.R., Bondre, N.R., Orem, C.A., Grant, G.E., Henry, C.D., 2012. Owyhee River
936 intracanyon lava flows: Does the river give a dam?. *GSA Bulletin*, 124(11–12), 1667–
937 1687. <http://dx.doi.org/10.1130/B30574.1>

938 Feng, M., Whitford-Stark, J.L., 1986. The 1719–1721 eruptions of potassium-rich lavas at
939 Wudalianchi, China, *Journal of Volcanology and Geothermal Research*, 30 (1–2),
940 131–148. [https://doi.org/10.1016/0377-0273\(86\)90070-3](https://doi.org/10.1016/0377-0273(86)90070-3)

941 Fuller, E.R., Head, J.W., 2002. Amazonis Planitia: The role of geologically recent volcanism
942 and sedimentation in the formation of the smoothest plains on Mars. *Journal of*
943 *Geophysical Research: Planets*, 107(E10). <http://dx.doi.org/10.1029/2002JE001842>

944 Galeczka, I., Sigurdsson, G., Eiríksdóttir, E.S., Oelkers, E.H., Gíslason, S.R., 2016. The
945 chemical composition of rivers and snow affected by the 2014/2015 Bárðarbunga
946 eruption, Iceland. *Journal of Volcanology and Geothermal Research*, 316, 101–119.
947 <http://dx.doi.org/10.1016/j.jvolgeores.2016.02.017>

948 Gíslason, S.R., Stefánsdóttir, G., Pfeffer, M.A., Barsotti, S., Jóhannsson, Th., Galeczka, I.,
949 Bali, E., Sigmarsson, O., Stefánsson, A., Keller, N.S., Sigurdsson, Á., Bergsson, B.,
950 Galle, B., Jacobo, V.C., Arellano, S., Aiuppa, A., Jónasdóttir, E.B., Eiríksdóttir, E.S.,
951 Jakobsson, S., Guðfinnsson, G.H., Halldórsson, S.A., Gunnarsson, H., Haddadi, B.,
952 Jónsdóttir, I., Thordarson, Th., Riishuus, M., Högnadóttir, Th., Dürig, T., Pedersen,
953 G.B.M., Höskuldsson, Á., Gudmundsson, M.T., 2015. Environmental pressure from
954 the 2014–15 eruption of Bárðarbunga volcano, Iceland. *Geochemical Perspectives*
955 *Letters*, 1(1), 84–93. <http://dx.doi.org/10.7185/geochemlet.1509>

956 Goff, J.R., Ashmore, P., 1994. Gravel transport and morphological change in braided
957 Sunwapta River, Alberta, Canada. *Earth Surface Processes and Landforms*, 19(3),
958 195–212. <http://dx.doi.org/10.1002/esp.3290190302>

959 Goldspiel, J.M., Squyres, S.W., 2000. Groundwater sapping and valley formation on
960 Mars. *Icarus*, 148(1), 176–192. <http://dx.doi.org/10.1006/icar.2000.6465>

961 Graettinger, A.H., Ellis, M.K., Skilling, I.P., Reath, K., Ramsey, M.S., Lee, R.J., Hughes,
962 C.G., McGarvie, D.W., 2013. Remote sensing and geologic mapping of glaciovolcanic
963 deposits in the region surrounding Askja (Dyngjufjöll) volcano, Iceland. *International*
964 *journal of remote sensing*, 34(20), 7178–7198.
965 <http://dx.doi.org/10.1080/01431161.2013.817716>

966 Gudmundsson, M.T., Jónsdóttir, K., Hooper, A., Holohan, E.P., Halldórsson, S.A., Ófeigsson,
967 B.G., Cesca, S., Vogfjörð, K.S., Sigmundsson, F., Högnadóttir, T., Einarsson, P.,
968 2016. Gradual caldera collapse at Bárðarbunga volcano, Iceland, regulated by lateral

969 magma outflow. *Science*, 353(6296), aaf8988,
970 <http://dx.doi.org/10.1126/science.aaf8988>

971 Gulick, V.C., 2001. Origin of the valley networks on Mars: A hydrological
972 perspective. *Geomorphology*, 37(3–4), 241–268. [http://dx.doi.org/10.1016/S0169-](http://dx.doi.org/10.1016/S0169-555X(00)00086-6)
973 [555X\(00\)00086-6](http://dx.doi.org/10.1016/S0169-555X(00)00086-6)

974 Gylfadóttir, S.S. 2016: Lágrennslisvísar. Greining þurrka og lágrennslímabila í nokkrum
975 vatnsföllum Landsvirkjunar. Icelandic Meteorological Office Report SSG/2016-01,
976 Reykjavík.

977 Hamilton, C., 2015. Team gets firsthand look at the new Holuhraun eruption site. *Eos*, 96,
978 [doi:10.1029/2015EO041197](https://doi.org/10.1029/2015EO041197).

979 Harrison, K.P., Grimm, R.E., 2005. Groundwater-controlled valley networks and the decline
980 of surface runoff on early Mars. *Journal of Geophysical Research: Planets*, 110(E12).
981 <http://dx.doi.org/10.1029/2005JE002455>

982 Hartley, M.E., Thordarson, T., 2013. The 1874–1876 volcano-tectonic episode at Askja,
983 North Iceland: Lateral flow revisited. *Geochemistry, Geophysics, Geosystems*, 14(7),
984 2286–2309. <http://dx.doi.org/10.1002/ggge.20151>

985 Hartley, M.E., T. Thordason, A. de Joux, 2016. Postglacial eruptive history of the Askja
986 region, North Iceland. *Bulletin of Volcanology*, 78, 28.
987 <http://dx.doi.org/10.1007/s00445-016-1022-7>

988 Higgins, C.G., 1982. Drainage systems developed by sapping on Earth and
989 Mars. *Geology*, 10(3), 147–152. [http://dx.doi.org/10.1130/0091-](http://dx.doi.org/10.1130/0091-7613(1982)10<147:DSDBSO>2.0.CO;2)
990 [7613\(1982\)10<147:DSDBSO>2.0.CO;2](http://dx.doi.org/10.1130/0091-7613(1982)10<147:DSDBSO>2.0.CO;2)

991 Hjartardóttir, Á.R., Einarsson, P., Gudmundsson, M.T., Högnadóttir, T., 2016. Fracture
992 movements and graben subsidence during the 2014 Bárðarbunga dike intrusion in

993 Iceland. *Journal of Volcanology and Geothermal Research*, 310, 242–252.
994 <http://dx.doi.org/10.1016/j.jvolgeores.2015.12.002>

995 Höskuldsson, A., Jónsdóttir, I., Thordarson, T., 2016. Futurevolc and the Bardarbunga
996 Eruption 2014–15 Iceland, Success in the Field and Laboratory. *European*
997 *Geosciences Union, General Assembly*, Vol. 18, Abstract EGU2016-13687.

998 Howard, A.D., Moore, J.M., Irwin, R.P., 2005. An intense terminal epoch of widespread
999 fluvial activity on early Mars: 1. Valley network incision and associated
1000 deposits. *Journal of Geophysical Research: Planets*, 110(E12).
1001 <http://dx.doi.org/10.1029/2005JE002459>

1002 Howard, D.A., Luzzadder-Beach S., Beach, T., 2012. Field evidence and hydraulic modeling
1003 of a large Holocene jökulhlaup at Jökulsá á Fjöllum channel, Iceland.
1004 *Geomorphology*, 147–148, 73–85. <http://dx.doi.org/10.1016/j.geomorph.2011.07.031>

1005 Huscroft, C.A., Ward, B.C., Barendregt, R.W., Jackson Jr, L.E., Opdyke, N.D., 2004.
1006 Pleistocene volcanic damming of Yukon River and the maximum age of the Reid
1007 Glaciation, west-central Yukon. *Canadian Journal of Earth Sciences*, 41(2), 151–164.
1008 <http://dx.doi.org/10.1139/e03-098>

1009 Ilyinskaya, E., Schmidt, A., Mather, T.A., Pope, F.D., Witham, C., Baxter, P., Jóhannsson, T.,
1010 Pfeffer, M., Barsotti, S., Singh, A., Sanderson, P., Bergsson, B., Kilbride, B.M.,
1011 Donovan, A., Peters, N., Oppenheimer, C., Edmonds, M., 2017. Understanding the
1012 environmental impacts of large fissure eruptions: Aerosol and gas emissions from the
1013 2014–2015 Holuhraun eruption (Iceland), *Earth and Planetary Science Letters*, 472,
1014 309–322. <https://doi.org/10.1016/j.epsl.2017.05.025>

1015 Jaeger, W.L., Keszthelyi, L.P., Skinner Jr, J.A., Milazzo, M.P., McEwen, A.S., Titus, T.N.,
1016 Rosiek, M.R., Galuszka, D.M., Howington-Kraus, E., Kirk, R.L., 2010. Emplacement

1017 of the youngest flood lava on Mars: A short, turbulent story. *Icarus*, 205(1), 230–243.
1018 <http://dx.doi.org/10.1016/j.icarus.2009.09.011>

1019 Jaenicke, J., Münzer, Ü., Minet, C., Eineder, M., Braun, L., Siegert, F., Gudmundsson, A.,
1020 2016. Volcanic activity at Bárðarbunga, Iceland, monitored with TerraSAR-X and
1021 TanDEM-X data, *TerraSAR-X/TanDEM-X Science Team Meeting*, Oberpfaffenhofen,
1022 Germany, 17–20 October 2016

1023 Jefferson, A., Grant, G.E., Lewis, S.L., Lancaster, S.T., 2010. Coevolution of hydrology and
1024 topography on a basalt landscape in the Oregon Cascade Range, USA. *Earth Surface
1025 Processes and Landforms*, 35(7), 803–816. <http://dx.doi.org/10.1002/esp.1976>

1026 Kiernan, K., Wood, C., Middleton, G., 2003. Aquifer structure and contamination risk in lava
1027 flows: insights from Iceland and Australia. *Environmental Geology*, 43(7), 852–865.
1028 <http://dx.doi.org/10.1007/s00254-002-0707-8>

1029 Kolzenburg, S., Jaenicke, J., Münzer, U., Dingwell, D.B., 2018. The effect of inflation on the
1030 morphology-derived rheological parameters of lava flows and its implications for
1031 interpreting remote sensing data – A case study on the 2014/2015 eruption at
1032 Holuhraun, Iceland. *Journal of Volcanology and Geothermal Research*, 357, 200–212.
1033 <https://doi.org/10.1016/j.jvolgeores.2018.04.024>

1034 Lamb, M.P., Howard, A.D., Johnson, J., Whipple, K.X., Dietrich, W.E., Perron, J.T., 2006.
1035 Can springs cut canyons into rock?. *Journal of Geophysical Research:
1036 Planets*, 111(E7). <http://dx.doi.org/10.1029/2005JE002663>

1037 Lanagan, P.D., McEwen, A.S., Keszthelyi, L.P. and Thordarson, T., 2001. Rootless cones on
1038 Mars indicating the presence of shallow equatorial ground ice in recent
1039 times. *Geophysical Research Letters*, 28(12), 2365–2367.
1040 <http://dx.doi.org/10.1029/2001GL012932>

- 1041 Lowe, D.J., Green, J.D., 1987. Origins and development of the lakes. In A. B. Viner (Ed.),
1042 *Inland Waters of New Zealand*, DSIR Bulletin, 241, 1–64. Wellington: New Zealand
1043 Department of Scientific and Industrial Research. <https://hdl.handle.net/10289/10555>
- 1044 Luo, W., Howard, A.D., 2008. Computer simulation of the role of groundwater seepage in
1045 forming Martian valley networks. *Journal of Geophysical Research: Planets*, 113(E5).
1046 <http://dx.doi.org/10.1029/2007JE002981>
- 1047 Maizels, J., 2002. 9 - Sediments and landforms of modern proglacial terrestrial environments.
1048 In *Modern and past glacial environments* 279–316. [http://dx.doi.org/10.1016/B978-](http://dx.doi.org/10.1016/B978-075064226-2/50012-X)
1049 [075064226-2/50012-X](http://dx.doi.org/10.1016/B978-075064226-2/50012-X)
- 1050 Mangold, N., Ansan, V., Masson, Ph., Quantin, C., and Neukum, G., 2008. Geomorphic study
1051 of fluvial landforms on the northern Valles Marineris plateau, Mars, *Journal of*
1052 *Geophysical Research*, 113, E08009. <https://doi.org/10.1029/2007JE002985>
- 1053 Marra, W.A., McLelland, S.J., Parsons, D.R., Murphy, B.J., Hauber, E. and Kleinhans, M.G.,
1054 2015. Groundwater seepage landscapes from distant and local sources in experiments
1055 and on Mars. *Earth Surface Dynamics*, 3(3), 389–408. [http://dx.doi.org/10.5194/esurf-](http://dx.doi.org/10.5194/esurf-3-389-2015)
1056 [3-389-2015](http://dx.doi.org/10.5194/esurf-3-389-2015)
- 1057 Melosh, H.J., 2011. *Planetary surface processes* (Vol. 13). Cambridge University Press,
1058 Cambridge, UK.
- 1059 Mounney, N.P., Russell, A.J., 2004. Sedimentology of cold-climate aeolian sandsheet
1060 deposits in the Askja region of northeast Iceland. *Sedimentary Geology*, 166(3–4).
1061 223–244, <http://dx.doi.org/10.1016/j.sedgeo.2003.12.007>
- 1062 Münzer, Ü., Jaenicke, J., Eineder, M., Minet, C., Braun, L., Mayer, C., Siegert, F., Franke, J.,
1063 2016. *Anwendung neuer Methoden mit hochauflösenden Fernerkundungs-daten*
1064 *(TerraSAR-X, TanDEM-X, RapidEye, UltraCam, HRSC) zur Früherkennung*
1065 *subglazialer Vulkanausbrüche auf Island, Final Report*, pp. 1–85.

1066 Nahm, A.L., Pendleton, M.W., Kattenhorn, S.A., 2016. Cerberus Fossae, Mars: The case for
1067 dike intrusion-related formation and modification. *Acta Geologica Sinica*, 90(1), 173–
1068 174. <http://dx.doi.org/10.1111/1755-6724.12957>

1069 Pauly, K., 2016. Trimble UX5 HP – Increasing Your Productivity. White Paper, Trimble
1070 Navigation Limited, 7pp. Available online at uas.trimble.com/media/downloads.

1071 Pedersen, G.B.M., Höskuldsson, A., Dürig, T., Thordarson, T., Jonsdottir, I., Riishuus, M.S.,
1072 Óskarsson, B.V., Dumont, S., Magnússon, E., Gudmundsson, M.T., Sigmundsson, F.,
1073 2017. Lava field evolution and emplacement dynamics of the 2014–2015 basaltic
1074 fissure eruption at Holuhraun, Iceland. *Journal of Volcanology and Geothermal*
1075 *Research*, 340, 155–169, <http://dx.doi.org/10.1016/j.jvolgeores.2017.02.027>

1076 Pelletier, J.D., Baker, V.R., 2011. The role of weathering in the formation of bedrock valleys
1077 on Earth and Mars: A numerical modeling investigation. *Journal of Geophysical*
1078 *Research: Planets*, 116(E11). <http://dx.doi.org/10.1029/2011JE003821>

1079 Pendleton, M.W., 2015. *Geomorphic evidence for geologically recent groundwater flow*
1080 *associated with the Cerberus Fossae magmatic and volcanic system, Mars*. MSc.
1081 Thesis, University of Idaho, 157 pp. ProQuest Dissertations Publishing. 1595198.

1082 Reynolds, H.I., Gudmundsson, M.T., Högnadóttir, T., Magnússon, E., Pálsson, F., 2017.
1083 Subglacial volcanic activity above a lateral dyke path during the 2014–2015
1084 Bárðarbunga-Holuhraun rifting episode, Iceland. *Bulletin of Volcanology*, 79(6), 38.
1085 <http://dx.doi.org/10.1007/s00445-017-1122-z>

1086 Richardson, J.A., Sutton, S., Whelley, P., Scheidt, S.P., Hamilton, C.W., Needham, D.H., and
1087 Bleacher, J.E., 2018. Repeat field campaigns at Holuhraun, Iceland: Exploring a new
1088 volcanic vent as a terrestrial analog for planetary surfaces. AGU Fall Meeting, 10–14
1089 December 2018, Washington DC, USA, Abstract P51C-10.

- 1090 Roach, I.C., Hill, S.M., Lewis, A.C., 2008. Evolution of a small intraplate basaltic lava field:
1091 Jerrabattgulla creek, upper shoalhaven river catchment, southeast New South
1092 Wales. *Australian Journal of Earth Sciences*, 55(8), 1049–1061,
1093 <http://dx.doi.org/10.1080/08120090802266543>
- 1094 Rossi, C., Minet, C., Fritz, T., Eineder, M., Balmer, R., 2016. Temporal monitoring of
1095 subglacial volcanoes with TanDEM-X – Application to the 2014–2015 eruption
1096 within the Bárðarbunga volcanic system, Iceland. *Remote Sensing of Environments*,
1097 181, 186-197, <https://doi.org/10.1016/j.rse.2016.04.003>
- 1098 Ruch, J., Wang, T., Xu, W., Hensch, M., Jónsson, S., 2016. Oblique rift opening revealed by
1099 reoccurring magma injection in central Iceland. *Nature Communications*, 7, 12352.
1100 <http://dx.doi.org/10.1038/ncomms12352>
- 1101 Sara, M.J., 2017. *Dyngjusandur sandsheet, Iceland, as a depositional analog to the Stimson*
1102 *Fm. in Gale Crater, Mars*. Doctoral dissertation, The University of Iowa, 145 pp.
- 1103 Sara, M. J., I. Ukstins Peate, M. S. Riishuus, R. A. Yingst, M. E. Schmidt, J. A. Berger, T.
1104 Hartsock, 2017. Askja sandsheet, Iceland, as a depositional analog for the Stimson
1105 Fm. in Gale Crater, Mars. In *Lunar and Planetary Science Conference (Vol. 48)*,
1106 Abstract 2638.
- 1107 Schorghofer, N., Jensen, B., Kudrolli, A., Rothman, D.H., 2004. Spontaneous channelization
1108 in permeable ground: Theory, experiment, and observation. *Journal of Fluid*
1109 *Mechanics*, 503, 357–374, doi:10.1017/S0022112004007931
- 1110 Self, S., L. Keszthelyi, T. Thordarson, 1998. The importance of pāhoehoe. *Annual Review of*
1111 *Earth and Planetary Sciences*, 26(1), 81–110,
1112 <https://doi.org/10.1146/annurev.earth.26.1.81>
- 1113 Sigmundsson, F., Hooper, A., Hreinsdóttir, S., Vogfjörð, K.S., Ófeigsson, B.G., Heimisson,
1114 E.R., Dumont, S., Parks, M., Spaans, K., Gudmundsson, G.B., Drouin, V., 2015.

1115 Segmented lateral dyke growth in a rifting event at Bárðarbunga volcanic system,
1116 Iceland. *Nature*, 517(7533), 191–195, <http://dx.doi.org/10.1038/nature14111>

1117 Stearns, H.T., 1936. Origin of the large springs and their alcoves along the Snake River in
1118 southern Idaho. *The Journal of Geology*, 44(4), 429–450.
1119 <http://dx.doi.org/10.1086/624441>

1120 Stearns, H.T., 1942. Hydrology of volcanic terranes. O.E. Meinzer (Ed.), *Hydrology*,
1121 McGraw-Hill, Toronto, Ont (1942), pp. 678-703

1122 Thordarson, T., Self, S., 1993. The Laki (Skaftár Fires) and Grímsvötn eruptions in 1783–
1123 1785. *Bulletin of Volcanology*, 55(4), 233–263, <http://dx.doi.org/10.1007/BF00624353>

1124 Thordarson, R., Larsen, G., Steinthorsson, S., Self, S., 2003. 1783–85AD Laki-Grímsvötn
1125 eruptions II: Appraisal based on contemporary accounts. *Jökull*; 51: 11-48.

1126 Thordarson, T. and Höskuldsson, Á., 2008. Postglacial volcanism in Iceland. *Jökull*, 58, 197–
1127 228.

1128 Voigt, J., Hamilton, C.W., Scheidt, S.P., Bonnefoy, L.E., Jónsdóttir, I., Höskuldsson, A.,
1129 Thordarson, T., 2017. Holuhraun 2014–2015 eruption site on Iceland: A flood lava
1130 analogue for Mars. In *European Planetary Science Congress* (Vol. 11), Abstract
1131 EPSC2017-848-1.

1132 Voigt, J.R.C. and Hamilton, C.W., 2018. Investigating the volcanic versus aqueous origin of
1133 the surficial deposits in Eastern Elysium Planitia, Mars, *Icarus*, 309, 389–410.
1134 <http://dx.doi.org/10.1016/j.icarus.2018.03.009>

1135 Woodruff, J.F. and Gergel, J., 1969. On the origin and headward extension of first-order
1136 channels, *Journal of Geography*, 68:2, 100–105,
1137 <https://doi.org/10.1080/00221346908981067>

1138
1139

1140

1141

1142

1143 **9. Tables and figures**

1144 *Table 1: Summary of the 2016, 2017, and 2018 field data in the hot springs region. For the*
 1145 *complete data, see Appendix B. Note these data were all taken between July 25 and August 4*
 1146 *of their respective years. The total discharge rate and heat flux given in this table correspond*
 1147 *only to that coming from the warm streams (including the warm half of mixed streams). The*
 1148 *area to the North of the old Jökulsá á Fjöllum riverbed is mainly covered by seepage channel,*
 1149 *so the last line of the table illustrates the coverage area of seepage channels. Since*
 1150 *groundwater level regulates seepage activity, this area gives an idea of relative groundwater*
 1151 *levels from year to year: unusually high in 2016, and low in 2017.*

	2015	2016	2017	2018
Total discharge rate from under the lava (m ³ /s)	–	9.3–14.0	2.2–4.3	3.0–5.2
Total heat flux from under the lava (GJ/s)	–	11.3–16.8	2.7–5.2	3.6–6.1
Stream area North of the old Jökulsá á Fjöllum riverbed in the hot springs region (m ²)	38,100	53,200	26,900	38,300

1152 * Dundas et al. (2017)

1153

1154

1155

1156

1157

1158 *Table 2: May–September values of the total monthly precipitation, for the years when data*
 1159 *was taken. Data is from ERA-Interim, which are a combination of worldwide model*
 1160 *predictions and nearby surface and satellite observations, and are given for the approximate*
 1161 *location of the 2014–2015 Holuhraun lava flow field (64.875°N, 16.500°W). See Section 3.4.*
 1162 *and Dee et al. (2011) for details on this dataset.*

	Total monthly precipitation (mm)				
	2003	2015	2016	2017	2018
May	67.9	72.8	27.2	116.7	105.9
June	71.3	42.7	40.6	87.0	60.9
July	113.3	88.5	70.2	54.3	76.9
August	44.4	126.6	81.7	42.2	89.6
September	82.2	91.0	158.6	178.0	82.5

1163

1164

1165 *Table 3: May–September values of monthly mean of daily mean temperature, for the years*
 1166 *when data was taken. The standard deviations, which are large because of day/night cycles,*
 1167 *are also given. Data is from ERA-Interim, which are a combination of worldwide model*
 1168 *predictions and nearby surface and satellite observations, and are given for the approximate*
 1169 *location of the 2014–2015 Holuhraun lava flow field (64.875°N, 16.500°W). See Section 3.4.*
 1170 *and Dee et al. (2011) for details on this dataset.*

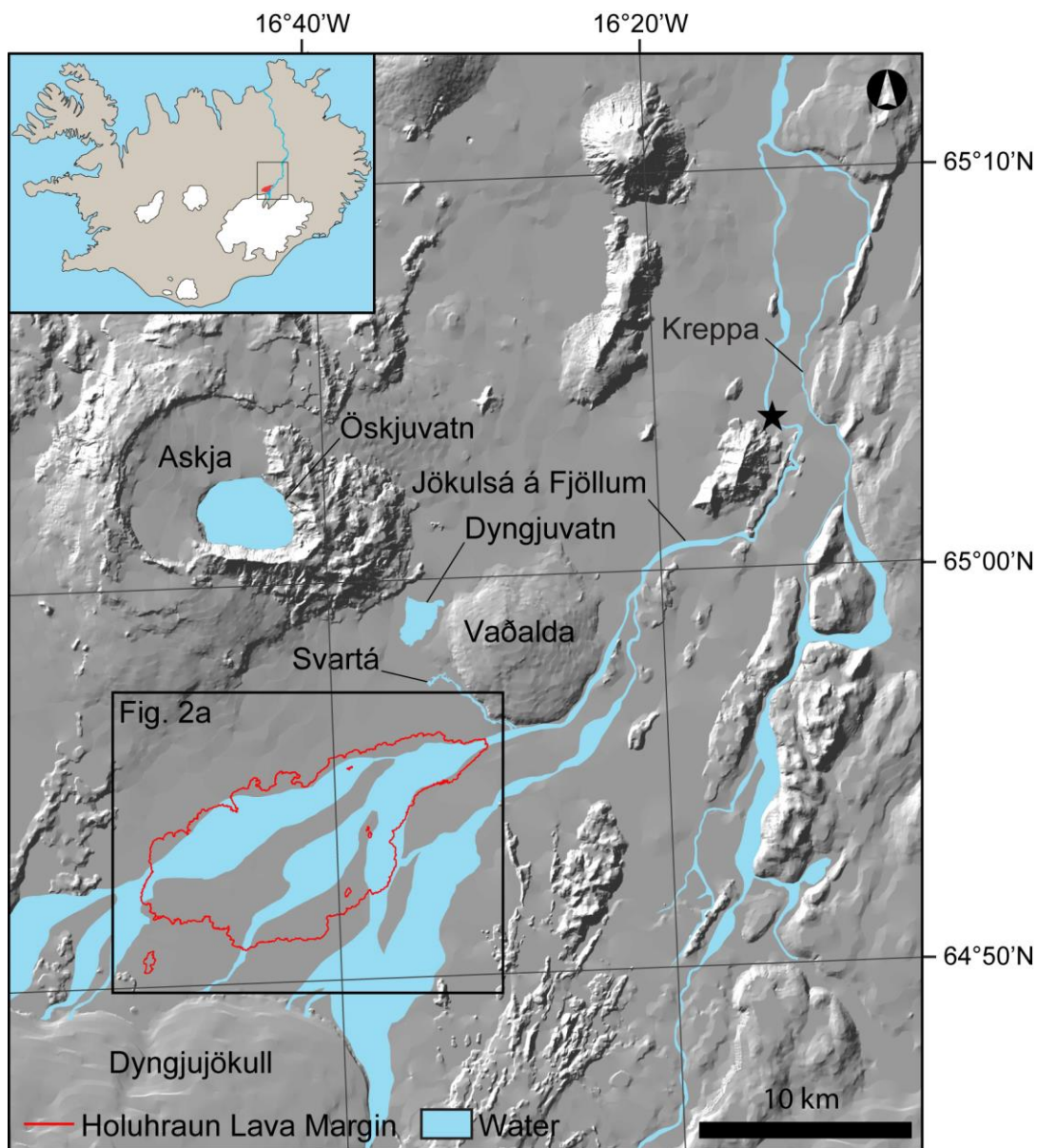
	Monthly mean of daily temperature (° C)				
	2003	2015	2016	2017	2018
May	-1.6±3.8	-2.7±3.8	-0.5±3.2	1.9±2.7	0.3±3.1
June	2.7±2.0	1.3±2.4	3.8±2.2	1.8±1.9	3.4±2.4

July	4.1±2.4	2.1±1.4	2.9±1.8	3.7±2.0	3.7±1.7
August	3.9±1.7	2.9±1.7	2.8±1.8	2.2±2.0	2.1±2.0
September	0.6±3.6	2.3±2.0	1.2±2.3	2.4±2.1	0.0±2.7

1171

1172

1173



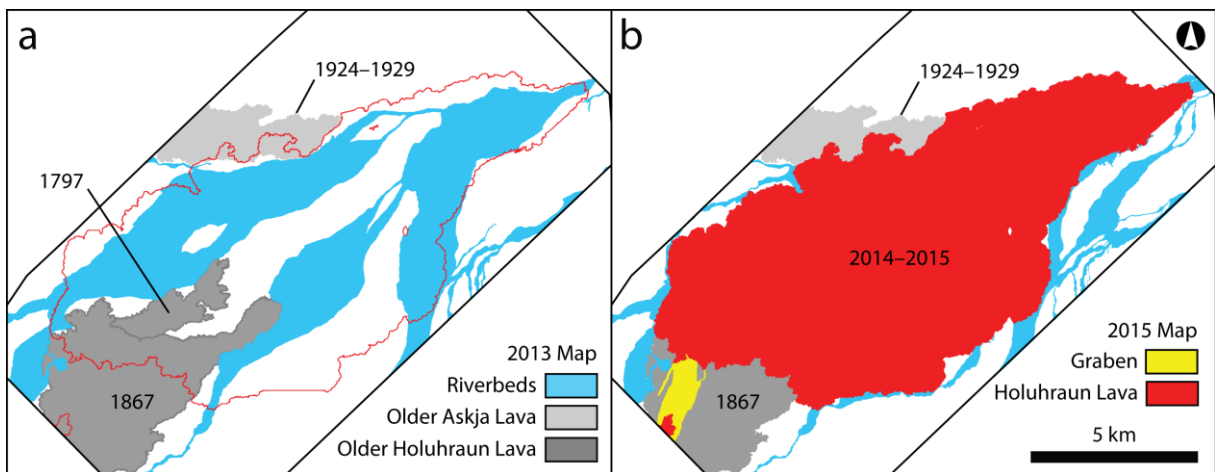
1174

1175

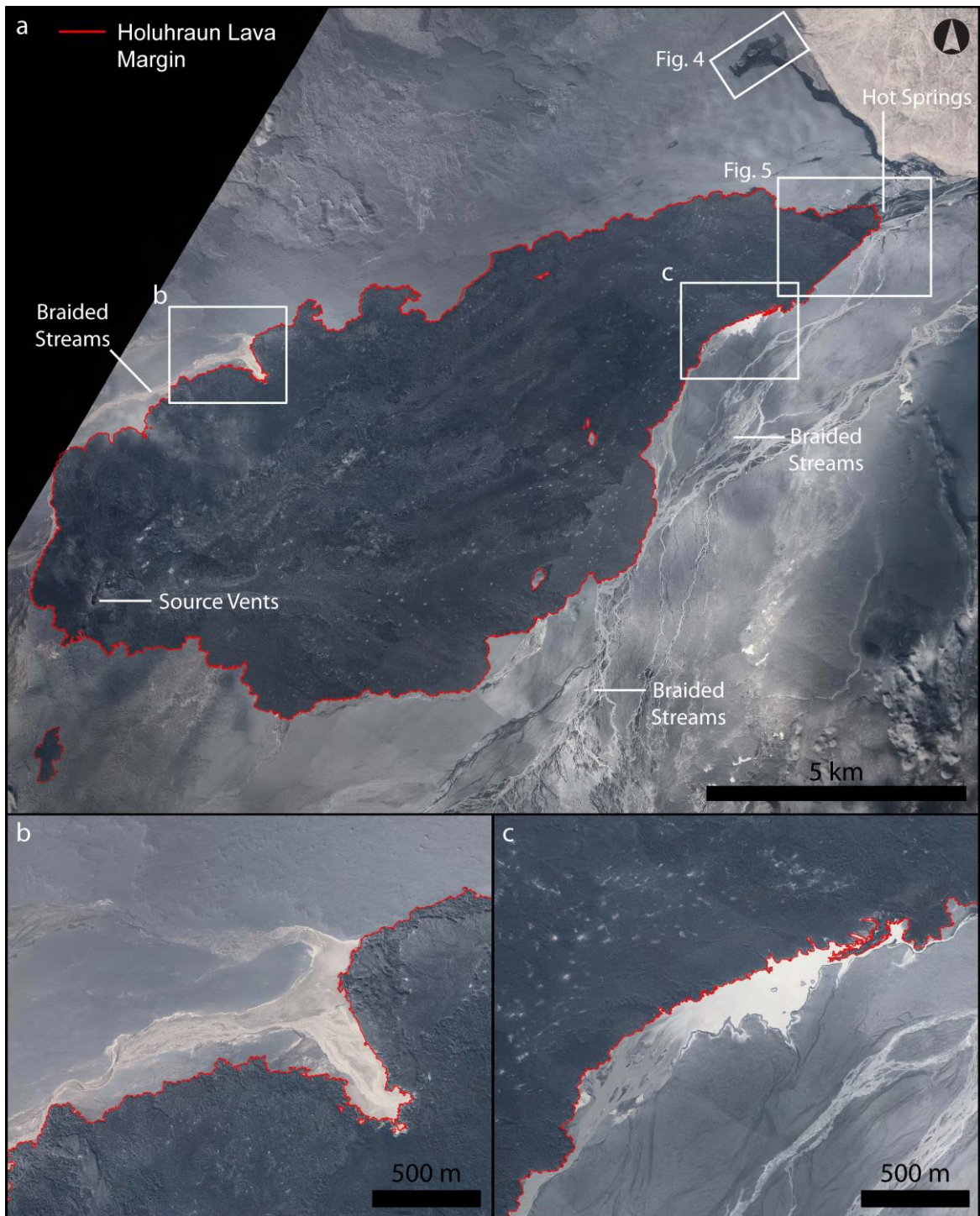
1176

Fig. 1: The region of interest, located north of the Vatnajökull ice cap. Main landmarks are named and the pre-eruption drainage patterns on Dyngjusandur are illustrated schematically.

1177 Also shown is the outline of the 2014–2015 Holuhraun lava flow field. Features were mapped
 1178 at a digitizing scale of 1:25,000. The background image is the IS50 hillshade from the
 1179 National Land Survey of Iceland. The location of the Upptyppingar gauging station is
 1180 indicated with a star. Inset shows the location of the figure within Iceland: it covers most of
 1181 Dyngjusandur and the Holuhraun lava field.
 1182



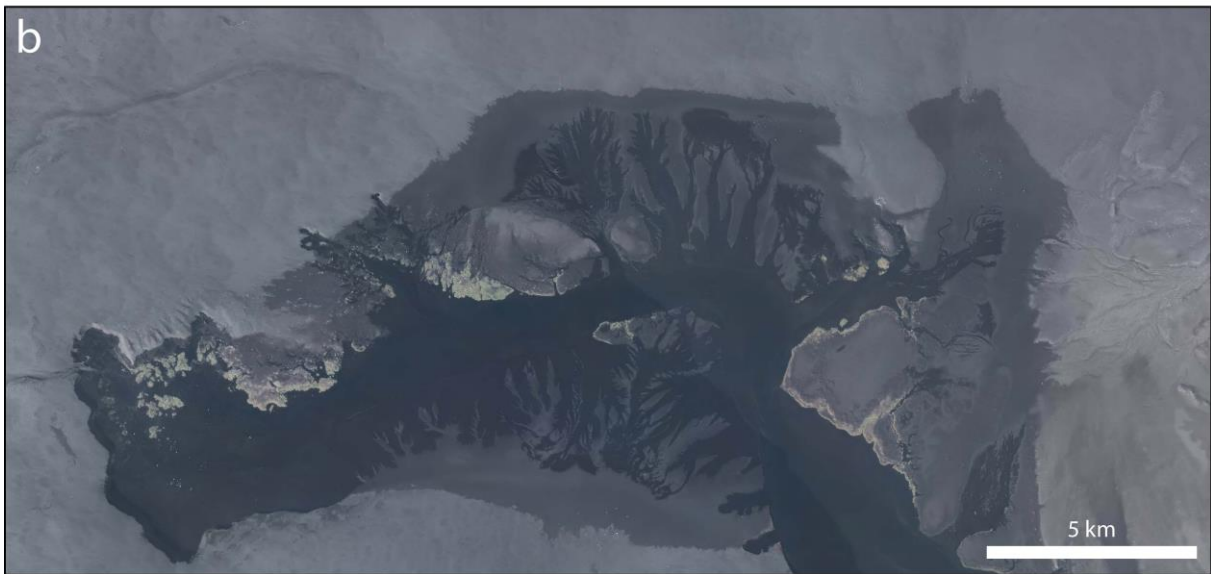
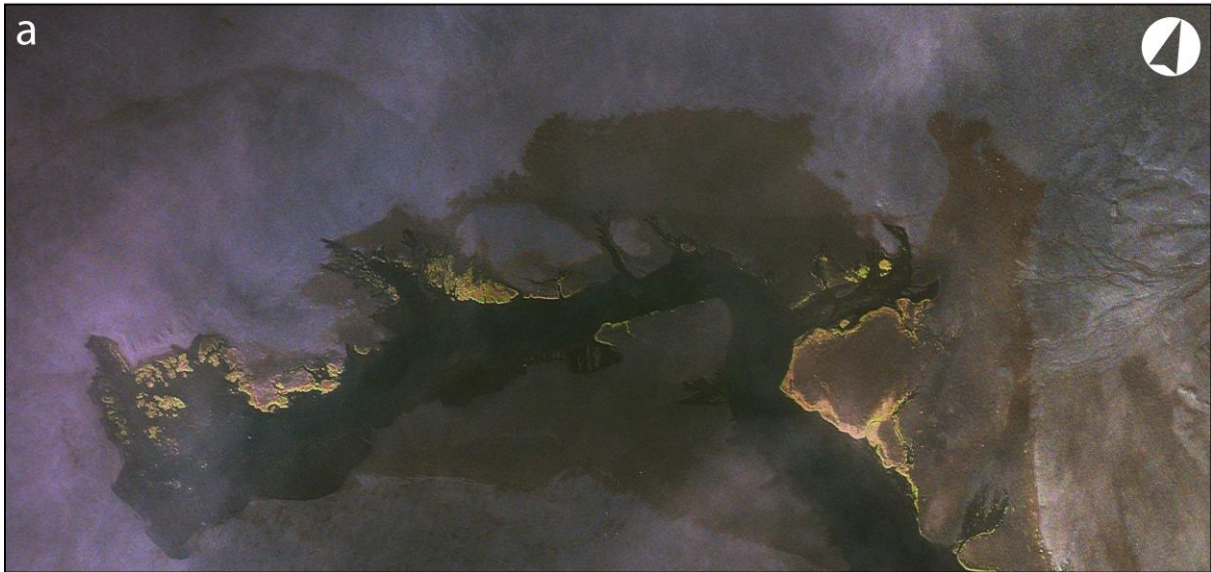
1183
 1184 Fig. 2: (a) Map of the pre-eruption landscape, showing the active riverbeds and lava flows
 1185 <300 years old. The 2014–2015 Holuhraun lava flow field is outlined in red. (b) Map of the
 1186 post-eruption landscape (2015). Features were mapped at a digitizing scale of 1:2,000.



1187

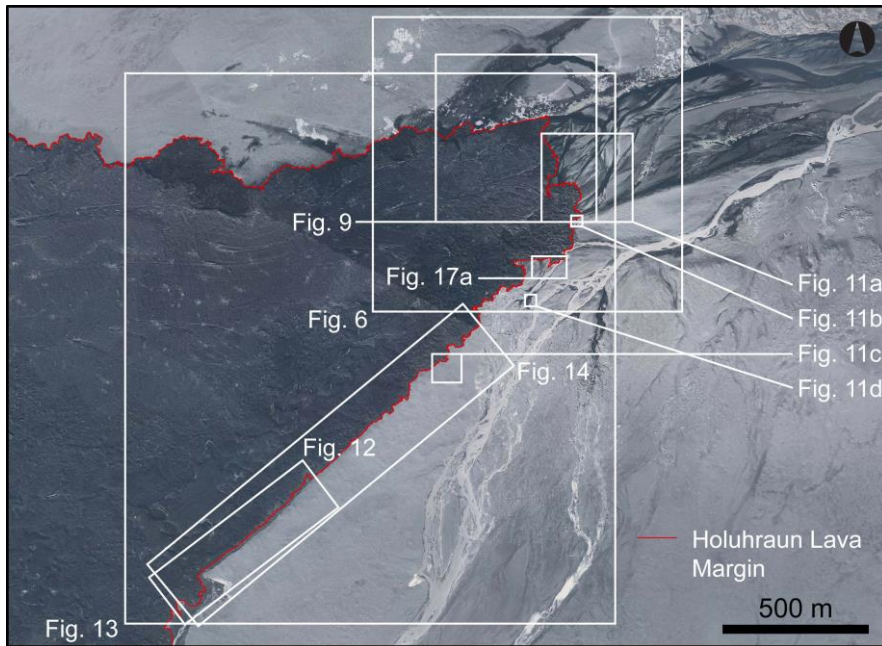
1188 *Fig. 3: (a) Detail of the lava flow and its surroundings in 2015, showing the location of two*
 1189 *proceeding figures. The lava flow field margins are shown in red. The background image is a*
 1190 *20 cm/pixel UltraCam-Xp true orthophotomosaic acquired on September 8, 2015 (IsViews,*
 1191 *LMU Munich). The two different lava-dammed lakes are shown in (b) and (c). (b) Detail of*
 1192 *the lava-dammed lake on the northwestern margin of the flow. This lake has changed little*

1193 *from 2016 to 2018. (c) Detail of the lava-dammed lake on the eastern margin of the flow field.*
1194 *This lake breached in July 2016; the stream now follows the margin of the lava into the hot*
1195 *springs region. The pale spots on the lava have been identified as thernadite, a sulfate, and*
1196 *indicate the position of fumerolic activity (Aufaristama et al., 2019).*



1197

1198 *Fig. 4: Source region for the Svartá seepage channel, showing its appearance in (a) August*
1199 *2014 (source: DigitalGlobe) and (b) September 2015 (UltraCam-Xp true orthophotomosaic,*
1200 *IsViews, LMU Munich). The height of headwalls in this region are approximately 6–8 m in*
1201 *height. The dark color of the sand surrounding Svartá is caused by water saturation, implying*
1202 *a shallow aquifer.*



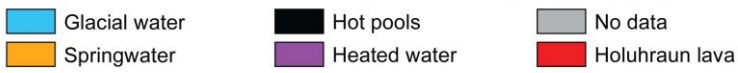
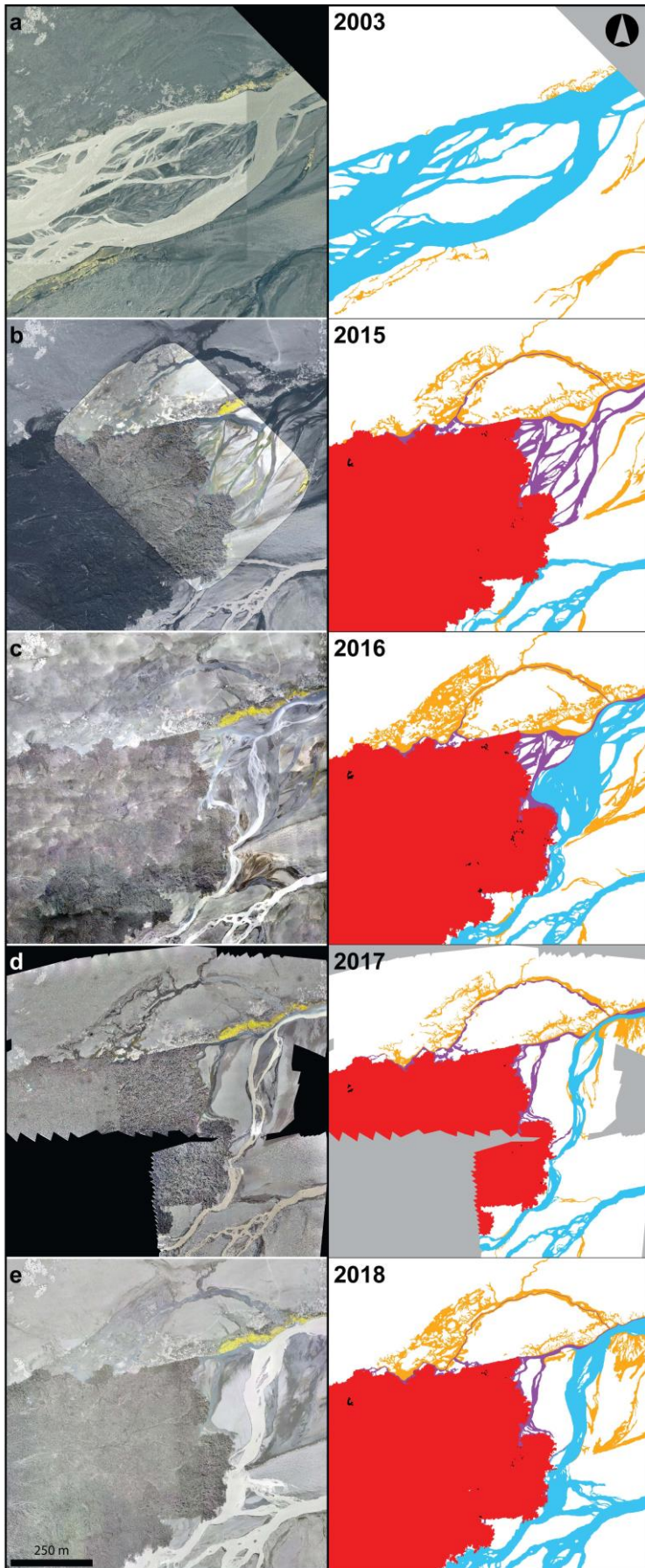
1203

1204 *Fig. 5: The distal end of the lava flow, showing the location of proceeding figures. The lava*

1205 *flow margin is shown in red. The background image is a 20 cm/pixel UltraCam-Xp true*

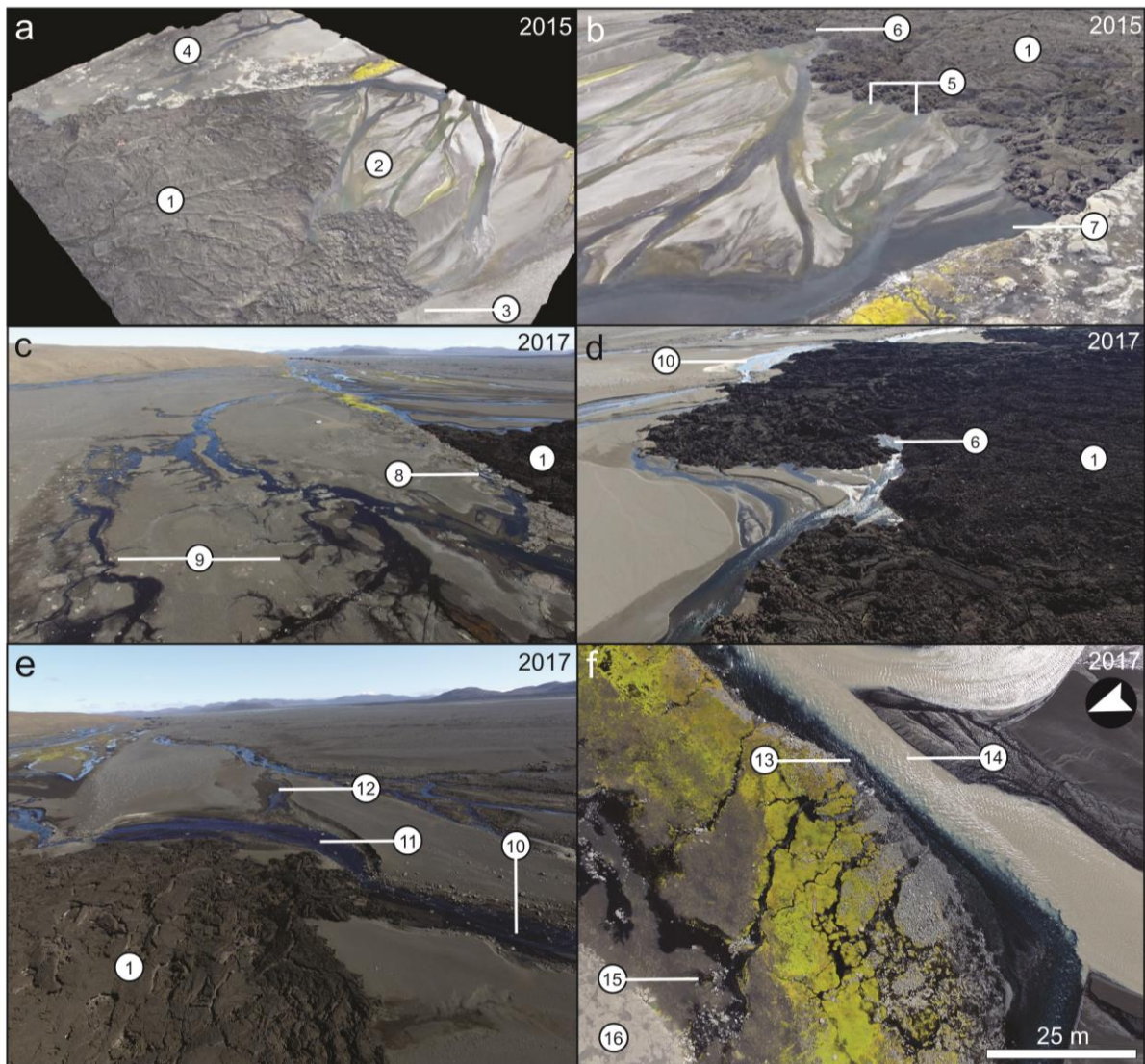
1206 *orthophotomosaic acquired on September 6, 2015 (IsViews, LMU Munich).*

1207



1209 *Fig. 6: Evolution of the hot springs region. Maps shown in the right column identify the*
1210 *locations of glacial water, springwater, hot pools, and heated water as well as the 2014–2015*
1211 *Holuhraun lava flow. These different water sources were inferred from temperature*
1212 *measurements as well as water flow directions; when several different sources merge, all*
1213 *colors are used in the channel. Note the development of seepage channels to the North, as*
1214 *well as the breakthrough of the glacial water into the hot springs region in 2016. Note also*
1215 *that every year, a small amount of heated water flows northward, but the cold seepage water*
1216 *dominates the temperature in these streams. Features were mapped at a scale of 1:300. (a) 50*
1217 *cm/pixel orthoimagery from Loftmyndir ehf. showing the landscape configuration in 2013. (b)*
1218 *2015, 4 cm/pixel orthoimagery acquired using a DJI Phantom 3 Pro sUAS, superimposed on*
1219 *20 cm/pixel UltraCam-Xp true orthophotomosaic (IsViews, LMU Munich). (c) 2016, 4*
1220 *cm/pixel orthoimagery acquired using a Trimble UX5-HP sUAS. (d) 2017, 2 cm/pixel*
1221 *orthoimagery acquired using a DJI Phantom 4 Pro sUAS. (e) 2018, 4 cm/pixel orthoimagery*
1222 *acquired using a Trimble UX5-HP sUAS.*

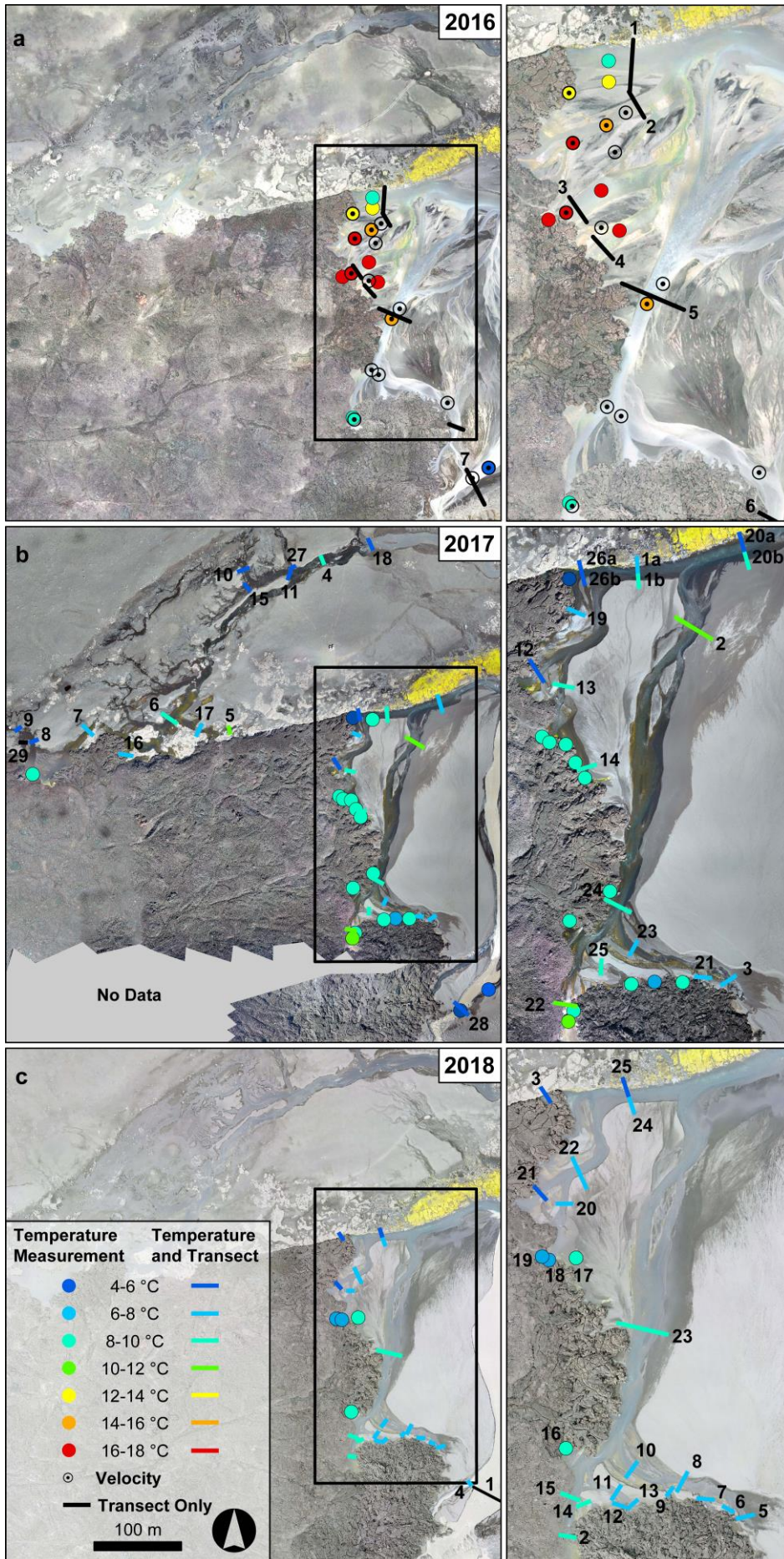
1223
1224



1225

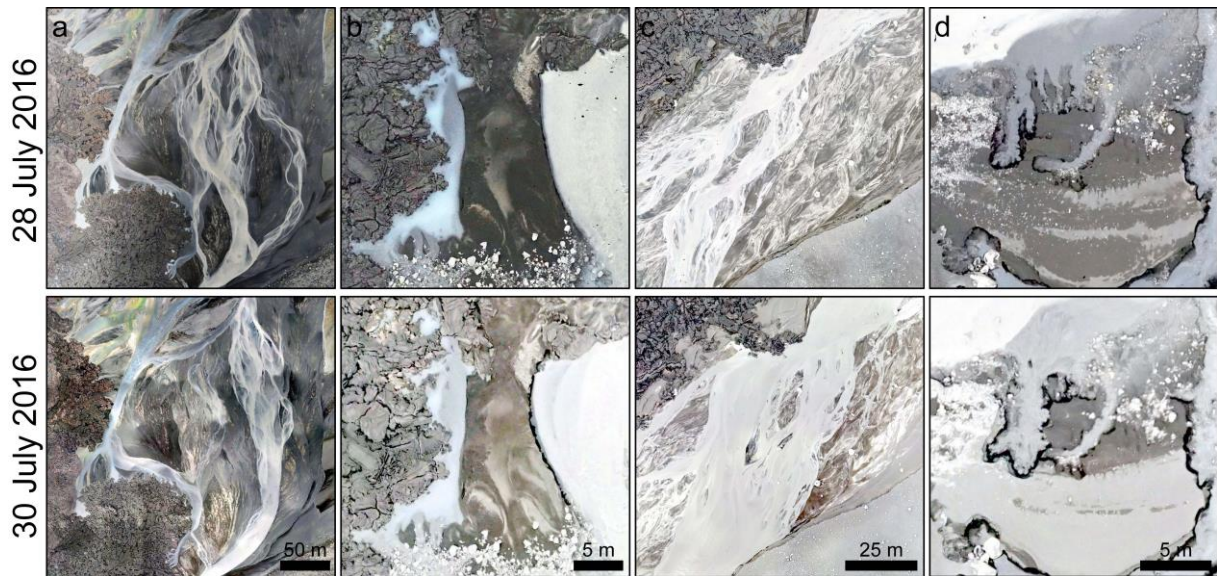
1226 *Fig. 7: (a) Perspective rendering of the hot springs region in 2015, facing north. 1: Northern*
1227 *portion of the 2014–2015 Holuhraun lava flow field. 2: Hot springs. 3: The margin of the lava*
1228 *abuts against the former margin of the river channel and in 2015, there were no overland*
1229 *flows of water at this locality. 4: Seepage channels exist in this region in 2015, and become*
1230 *more pronounced over the following year. (b) Perspective rendering of the hot springs region in*
1231 *2015, facing south. 5: In 2015, the warmest hot spring branches had the most algae and were*
1232 *greener. 6: Location of a warm pool. 7: Cool water dominantly fed along the margin, rather*
1233 *than through, the lava. (c) Perspective view of the northern margin of the lava in 2017, facing*
1234 *northeast. 8: Water, largely from seepage channels, flows along the margin of the lava*

1235 *toward the hot springs region, emerging at the location identified by 7. 9: Active seepage*
1236 *channels. (d) Perspective view of the northern margin of the lava in 2017, facing south. 10:*
1237 *Location of the stream branch formed during the 2016 dam-breaching event, which carved a*
1238 *new channel along the eastern margin of the lava, transporting glacial meltwater into the hot*
1239 *springs region. Note this is the same location as 3. (e) Perspective view of the glacial*
1240 *meltwater streams on the eastern side of the lava flow in 2017. 10 and 11: channel formed in*
1241 *2016 feeding water toward the location of the hot springs. 12: Spillway channel connecting to*
1242 *another branch of the Jökulsá á Fjöllum river. When there is too little glacial melt to reach*
1243 *this channel, seepage is observed there. (f) Nadir-pointing view of a mixing zone north of the*
1244 *former hot springs region in 2017. Here, clear water (13), which is a mixture of seepage*
1245 *spring and lava filtered water, merges with sediment laden glacial river water (14). 15: Small*
1246 *seepage channels. 16: Old lava flow surfaces; these are also visible in 4.*



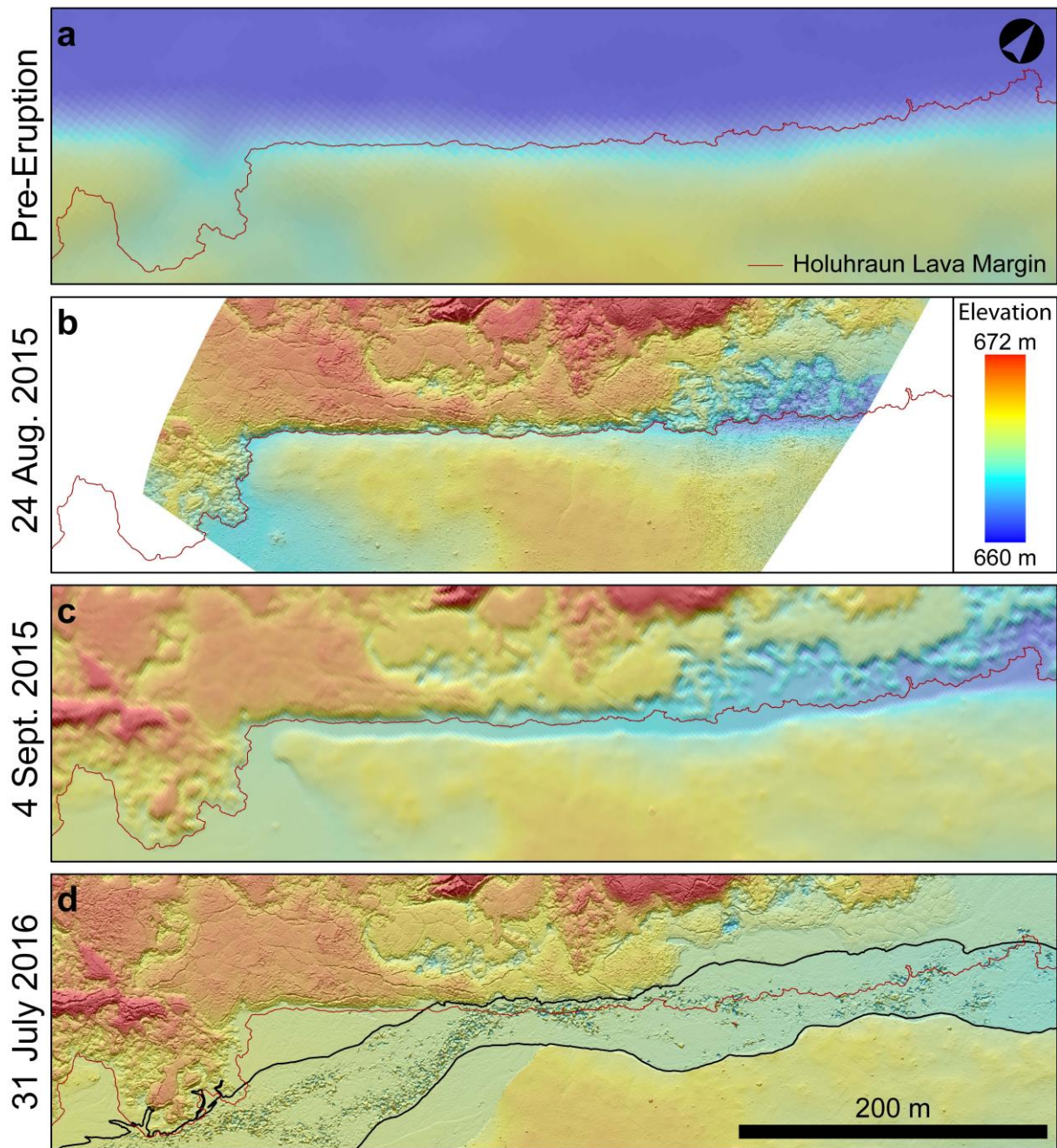
1248 *Fig. 8: Location of the hydrology measurements taken in the hot springs region in 2016,*
1249 *2017, and 2018. Temperature is shown where available. All corresponding data and*
1250 *coordinates are given in Appendix B. The transects are numbered for reference in tables B1–*
1251 *B3. (a) Map of the sUAS and field data gathered in the hot springs region during July 2016.*
1252 *In 2016, temperature and velocity were measured at select points, and the depth profile*
1253 *across each stream was measured independently. Consequently, the temperature and velocity*
1254 *are only an approximation at the location of the transects. The background is a 4 cm/pixel*
1255 *orthoimage taken on 7/30/2016 using the Trimble UX5-HP. (b) Map of the sUAS and field*
1256 *data gathered for the same region during July 2017. In 2017, water temperature and velocity*
1257 *were measured within each cross-section. The background is a 2–3 cm/pixel orthoimage*
1258 *taken on 7/25–28/2017 using the DJI Phantom 4 Pro quadcopter. (c) Map of the sUAS and*
1259 *field data gathered in the hot springs region during August 2018. In 2018 also, water*
1260 *temperature and velocity were measured within each cross-section. The background is a 4*
1261 *cm/pixel orthoimage taken on 8/3/18 using the Trimble UX5-HP. Note the glacial stream in*
1262 *transect #1 has highly variable temperature, which are therefore not shown here.*

1263



1264

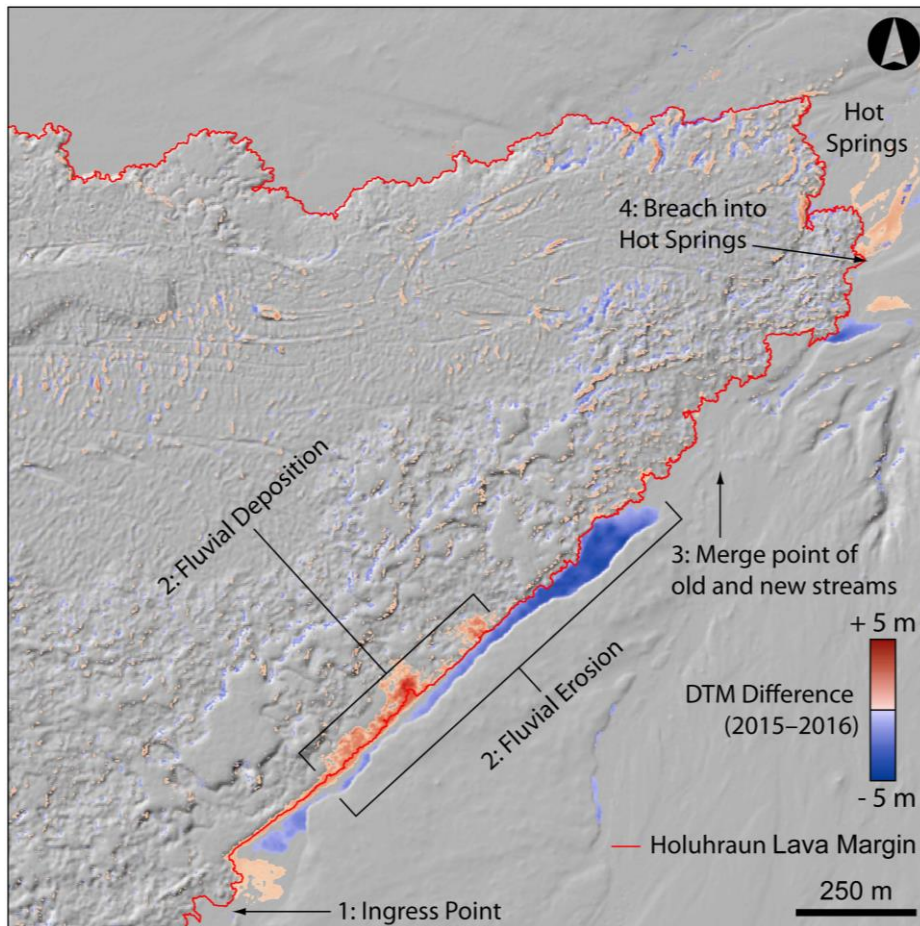
1265 *Fig. 9: Changes observed between July 28 and July 30, 2016. Top: 1 cm/pixel orthoimage*
1266 *acquired by a Trimble UX5-HP sUAS on July 28. Bottom: 4 cm/pixel orthoimage using the*
1267 *same sUAS on July 30. (a) Braided stream morphological changes. (b) Channel bank erosion.*
1268 *(c) Water level variations in the glacial river. (d) Seepage channel development.*



1269

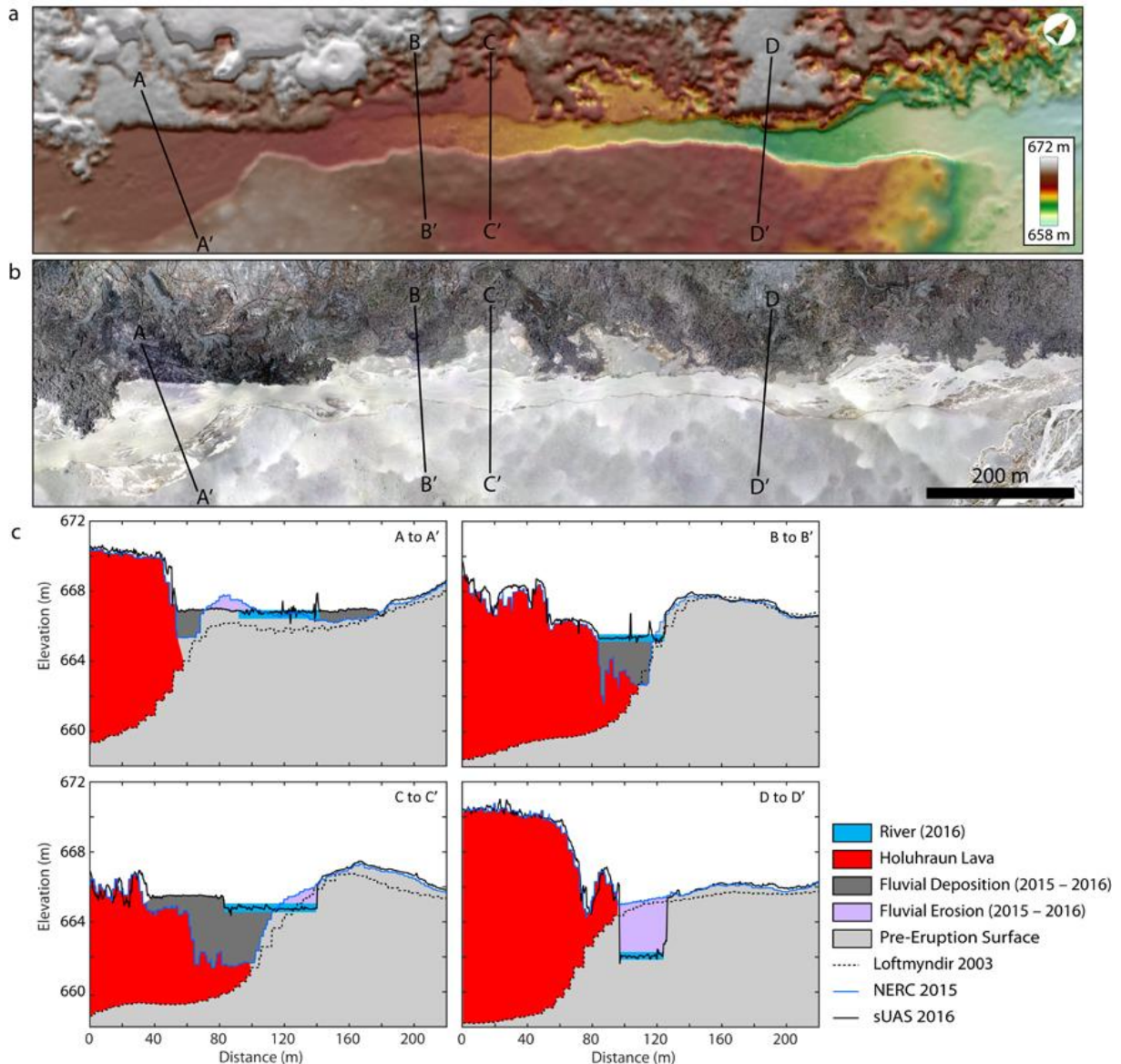
1270 *Fig. 10: Evolution of the region just downstream of the lake that breached in 2016. (a)*
 1271 *Topography showing the right bank of a branch of the Jökulsá á Fjöllum river prior to the*
 1272 *emplacement of the 2014–2015 Holuhraun lava flow field. The riverbank was about 10 m*
 1273 *high at this location. (b) In 2015, lava entered the river channel and abutted against its*
 1274 *banks. (c) Between August 24 and September 4, 2015, the lake which had formed just west of*
 1275 *this region overflowed, causing both erosion and some sediment deposition. The water did not*
 1276 *reach the main channel, and the landscape is dry on September 4. (d) Water from the lake*

1277 *developed an overland flow toward the hot springs region forming a connection on July 21. A*
1278 *major dam-breaching event then occurred on July 22, 2016, transporting large amounts of*
1279 *sediment into the river and onto the lava flow. A branch of the Jökulsá á Fjöllum now goes*
1280 *through this region, including on top of the new lava. Note that reflections on the water within*
1281 *the Jökulsá á Fjöllum causes large amounts of noise in the resulting MVSP-derived DTM.*



1282

1283 *Fig. 11: Elevation changes from 2015 to 2016 in the hot springs region, obtained by*
 1284 *subtracting the 2015 topography (NERC LiDAR and Loftmyndir photogrammetry; 2–5*
 1285 *m/pixel) from the 2016 topography (Trimble sUAS DTM; 20 cm/pixel), degraded to the same*
 1286 *resolution. Elevation changes smaller than ± 0.7 m are not shown. The background is a*
 1287 *hillshade created from the 20 cm/pixel DTM taken in 2016. The outline of the 2014–2015*
 1288 *Holuhraun lava flow is shown in red. The apparent small elevation changes within the lava*
 1289 *flow field are not real: they are due to small errors in the georeferencing of the DTMs. The*
 1290 *sequence of events of the dam breach is indicated. 1: The lake breached approximately at this*
 1291 *point. 2: The dam breaching event entrenched a new channel and deposited sediment onto the*
 1292 *lava. 3: The new stream running along the lava merged with the older stream, which reached*
 1293 *this point through another route. 4: The added water was enough to breach through the old*
 1294 *riverbank and into the hot springs.*



1295

1296

1297

1298

1299

1300

1301

1302

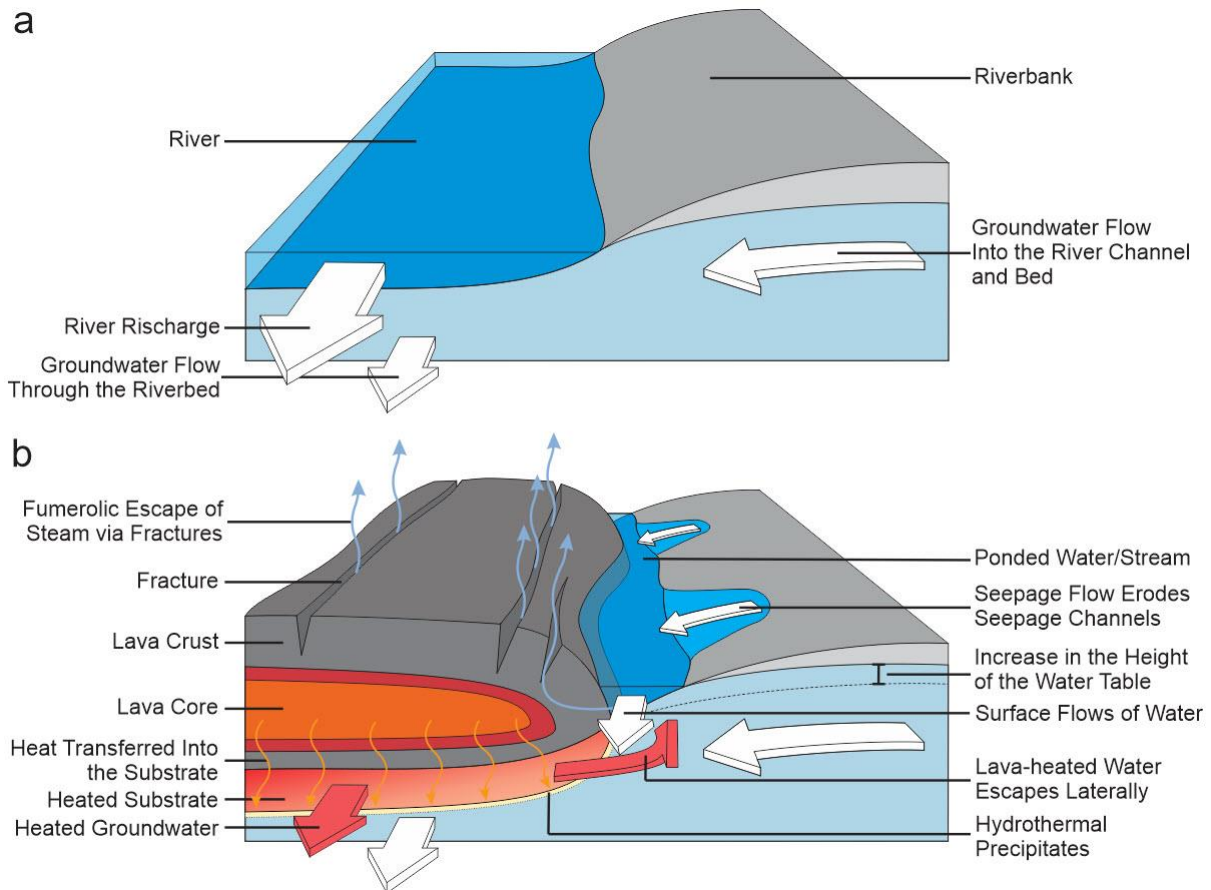
1303

1304

Fig. 12: We show (a) the 4 cm/pixel 2016 sUAS DTM, and (b) the 4 cm/pixel 2016 sUAS orthoimage, of the lava flow margin downstream of the lava-dammed lake that breached on 22 July 2016, one week after the breach. Elevation profiles were taken every meter along the new bed of the Jökulsá á Fjöllum river; four of these profiles are taken as examples. (c) Topography profiles are taken from the following datasets: the 2003 DTM from Loftmyndir ehf., the 2015 Lidar data from NERC, and the 2016 DTM from the Trimble UX5-HP sUAS. The lava, older glacial sediment, and position of the river in 2016 are shown. Regions of confirmed sediment deposition and erosion having occurred during the dam breaching event (i.e., between the time the 2015 and 2016 data were taken) are pointed out. Note the UAS data

1305 *is noisier in the river due to reflections from the water in the images. The 2003 DTM may be*
 1306 *offset by ± 0.5 meters in this region (see Appendix A). Of these four examples, flood channel*
 1307 *depth and width can only be estimated for profiles 634 and 1100 (on the right).*

1308
 1309
 1310



1311
 1312 *Fig. 13: Illustration of the surface and groundwater flow before and after the emplacement of*
 1313 *the lava. (a) The river before emplacement of the lava flow. Seepage activity near the river*
 1314 *was limited before the eruption and is not included here. (b) The lava was emplaced in the*
 1315 *riverbed. The subsequent increase in the height of the water table caused ponding and the*
 1316 *formation of seepage channels along the banks. The lava-heated water escapes both into the*
 1317 *stream that forms along the bank, and at the distal end of the lava in the hot springs. A thin*
 1318 *layer of hydrothermal precipitates might be present, isolating the groundwater flows inside*
 1319 *and outside the lava.*

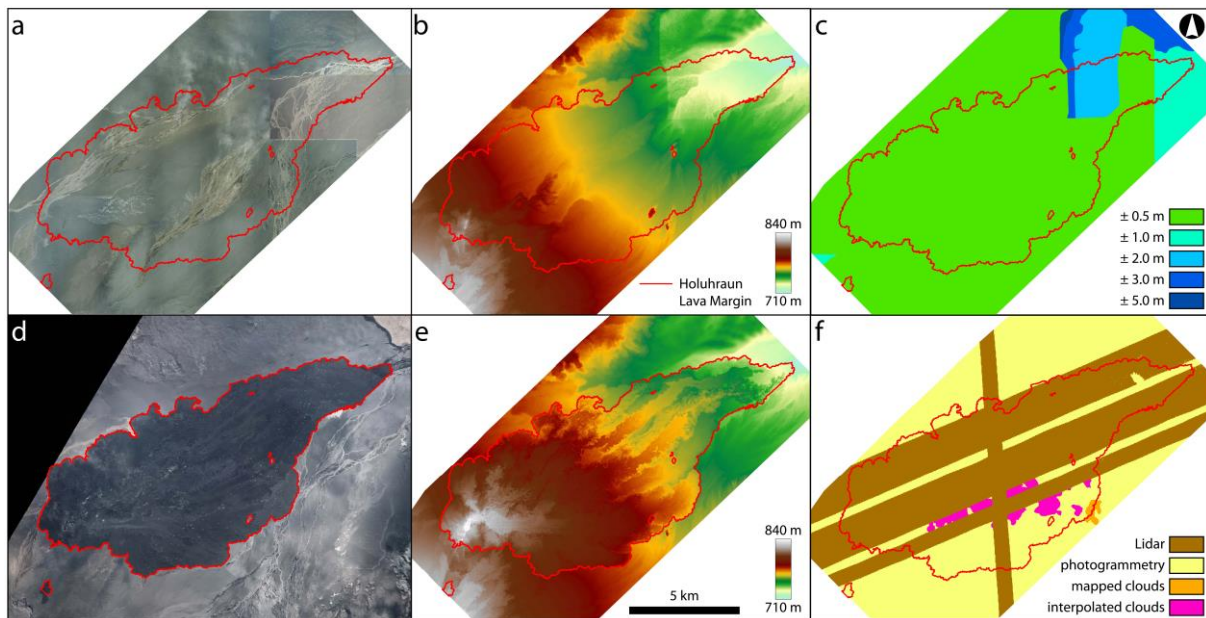
1320

1321

1322 **Appendix A: Coverage and Resolution of Airborne Remote Sensing Data**

1323 In our study, we use airborne remote sensing data collected during the summers of
1324 2003, 2013, 2015, 2016, 2017, and 2018. These data are described in Section 3.1 and detailed
1325 information is given in Table A1. Fig. A1 shows the extent and resolution of the pre- and
1326 post-eruption datasets covering the entirety of the Holuhraun lava flow field.

1327



1328 *Fig. A1: Top: Pre-eruption dataset, taken in August 2003 and August 2013 and processed by*
1329 *Loftmyndir ehf. Bottom: Post-eruption regional dataset, dating from August 2015. This*
1330 *dataset includes data from NERC, Loftmyndir ehf., and the IsViews Project.*

1332

1333

1334

1335

1336

1337 *Table A1: Characteristics of the aerial data used.*

Year	Date	Data Type	GSD	Areal Coverage	Platform	Processed
2003	23 Aug.	Orthophoto-mosaic	50 cm	35.6 km ² ; future hot spring region	Airborne photogrammetry	Loftmyndir ehf.
		DTM	5 m			
2013	12 Aug	Orthophoto-mosaic	50 cm	130.6 km ² ; lava field and surroundings	Airborne photogrammetry	Loftmyndir ehf.
		DTM	5 m			
2015	24 Aug.	Orthophoto-mosaic	4 cm	0.14 km ² ; dam breaching region	sUAS (Phantom 3 Pro)	Pix4D
		DTM	16 cm			
	30 Aug.	Orthophoto-mosaic	50 cm	167 km ² ; lava field and surroundings	Airborne photogrammetry	Loftmyndir ehf.
		DTM	5 m			
	4 Sept.	DTM	2 m	100 km ² ; partial coverage of lava field and surroundings	Airborne LiDAR	NERC
	4 Sept.	Orthophoto-mosaic	4 cm	0.24 km ² ; hot spring region	sUAS (Phantom 3 Pro)	Pix4D
DTM		16 cm				
8 Sept.	Orthophoto-mosaic	20 cm	837 km ² ; lava field, Vaðalda, Svartá, Askja, Vatnajökull	Airborne UltraCam	IsViews, LMU Munich	
2016	28 July	Orthophoto-mosaic	1 cm	0.96 km ² ; hot springs region	sUAS (UX5-HP)	Trimble Business Center
		DTM	5 cm			
	30–31 July	Orthophoto-mosaic	4 cm	8.2 km ² ; hot springs region	sUAS (UX5-HP)	Trimble Business Center
		DTM	20 cm			
2017	25–28 July	Orthophoto-mosaic	2.3 cm	0.76 km ² ; hot springs region	sUAS (Phantom 4 Pro)	Pix4D
		DTM	9 cm			
2018	3 Aug.	Orthophoto-mosaic	4 cm	8.2 km ² ; hot springs region	sUAS (UX5-HP)	Trimble Business Center
		DTM	20 cm			

1338

1339

1340 *Table A2: Precision of UAV data products. UX5-HP data products are georeferenced using*
1341 *differentially corrected GPS data from an R10 base station and the UX5-HP's GNSS GPS*
1342 *receiver. The R10 dGPS is capable of producing survey points with excellent precision (0.8*
1343 *cm horizontal and 1.5 cm vertical). This allows calculation of the plane's exact flight paths.*
1344 *Combined with the exact timing of the camera shutter, the positions of each image acquisition*
1345 *is known during the flight path and are therefore airborne control points. The mean standard*
1346 *deviations (at $\pm 1\sigma$) in the x, y, and z directions (i.e., latitude, longitude, and elevation) of*
1347 *terrain points for 2016 are estimated to be ± 3.0 cm, ± 4.0 cm, and ± 6.4 cm, respectively. For*

1348 2018, these values are ± 4.1 cm, ± 3.1 cm, and ± 5.8 cm, respectively. Phantom sUAS surveys
 1349 are coregistered using ground control tie points visible in 2016 UX5-HP orthoimage data;
 1350 height values are obtained from the DTM. For co-registered Pix4D-processed surveys, the
 1351 table below reports the mean root mean square error (RMSE) of terrain points as compared
 1352 to control points used from 2016 UX5-HP orthoimage and DTM data.

Year	Day	Platform	Control Method	No. of Control Points	RMSE (cm)
2015	24 Aug.	Phantom 3 Pro	Manual coregistration of tie points to 2016 UX5-HP data	7	10.6
2015	4 Sept.	Phantom 3 Pro	Manual coregistration of tie points to UX5-HP data	7	2.70
2017	25–28 July	Phantom 3 and 4 Pro	Manual coregistration of tie points to UX5-HP data	16	3.50

1353

1354 **Appendix B: hydrology analysis methods**

1355 **B.1. 2016 hydrological analysis**

1356 In 2016, channels profiles were measured using a Trimble R10 DGPS, with 3-cm-
 1357 precision, which was used to sample the depth of the channel every 10–20 cm. A Hydrolab
 1358 DS5 Multiparameter Data Sonde was used to measure a variety of parameters associated with
 1359 each stream channel, including temperature and pH, which were measured with a precision of
 1360 0.01°C, and 0.01 pH units, respectively. A General Oceanics, Inc. Environmental flow
 1361 meter/velocity sensor was used to measure water flow velocity with a precision of 0.1 m/s.
 1362 Water flux Q [m³/s] was determined for each channel by calculating the channel cross-
 1363 sectional area and multiplying by corresponding velocity measurement. Heat flux, E_{flux} [J/s],
 1364 was then calculated using Equation 2. In 2016, temperature and velocity data were taken on
 1365 different days and in some places are offset from the transects. We therefore used the nearest
 1366 velocity and temperature point within the same stream for each transect. Note that cross-
 1367 sections #6 has no nearby temperature and pH measurement, and cross-section #1 has no
 1368 nearby velocity measurement.

1369

1370 *Table B1: Results of the field data gathered in the hot springs region between July 28 and*
 1371 *August 4, 2016. If several temperature and velocity measurements were taken for a stream,*
 1372 *the average is presented here. For cross-section #1, no velocity measurements were taken; we*
 1373 *therefore calculated the velocity using Manning’s equation, as described in Section 3.3. In*
 1374 *cross-section #6, no temperature or pH measurements were taken. Given that cross-section*
 1375 *#6 has the same water source as cross-section #7, we assume the same water temperature*
 1376 *when calculating the heat flux. We also note that cross-section #1 is a mixture of cold*
 1377 *springwater and water heated by the lava. See Fig. 6a for a map of these data. Latitude and*
 1378 *longitude are referenced to the Islands Net 2004 datum.*

ID	Channel type	Cross-Sectional Area (m ²)	Temperature (°C)	pH	Velocity (m/s)	Discharge Rate (m ³ /s)	Heat Flux (GJ/s)	Start Longitude	Start Latitude	End Longitude	End Latitude
1	Mixed	6.1	8.7	8.9	0.77*	4.7	5.56	-16.513326	64.932474	-16.513260	64.932737
2	Hot springs	2.1	14.8	8.8	0.92	1.9	2.31	-16.513303	64.932445	-16.513171	64.932347
3	Hot springs	3.2	16.9	8.7	0.47	1.5	1.81	-16.513937	64.931831	-16.514103	64.931936
4	Hot springs	2.6	16.7	8.7	0.71	1.9	2.26	-16.513638	64.931632	-16.513839	64.931738
5	Hot springs	3.5	13.5	8.8	1.15	4.0	4.87	-16.512978	64.931392	-16.513303	64.931451
6	Glacial	7.0	_**	_**	0.68	6.2	7.29	-16.511678	64.930236	-16.511928	64.930273
7	Glacial	8.4	5.7	7.8	1.25	8.6	10.16	-16.511529	64.929794	-16.511335	64.929609

1379 * Calculated

1380 ** No data available; we assume the same values as for stream #7

1381

1382 **B.2. 2017 Hydrological Analysis**

1383 In 2017, stream profiles were also measured, but in a different way to account for
 1384 variable conditions across the streams. For each stream cross-section shown in Fig. 8b, stream
 1385 depths were measured using a tape measure at regular intervals, ranging from 20 cm to 1 m,
 1386 with depth measurements rounded to the nearest centimeter. For each measured segment
 1387 along the stream profile we measured temperature and pH using an Ecosense pH10A

1388 Handheld pH/Temperature Pen Tester, which has a precision of 0.01°C, and 0.01 pH units,
 1389 respectively. Stream flow velocities were measured with Global Water Flow Probe, with a
 1390 precision of 0.1 m/s. We then calculated Q and E_{flux} in each segment of the stream (see
 1391 Equations 1 and 2), which we then summed to obtain the total discharge rate and total heat
 1392 flux through each stream.

1393

1394 *Table B2: Results of the field data gathered in the hot springs region in July 2017. If several*
 1395 *temperature and velocity measurements were taken for a stream, the average is presented*
 1396 *here. Cross-section #29 was too shallow for temperature and pH measurements to be taken.*
 1397 *We also note that cross-sections #1, 4, 6, 7, 18, 20, and 26 are mixtures of cold springwater*
 1398 *and water heated by the lava. See Fig. 8b for a map of these data. Latitude and longitude are*
 1399 *referenced to the Islands Net 2004 datum.*

ID	Channel type	Cross-Sectional area (m ²)	Temperature (°C)	pH	Velocity (m/s)	Discharge Rate (m ³ /s)	Heat Flux (GJ/s)	Start Longitude	Start Latitude	End Longitude	End Latitude
1a	Cold spring	1.6	6.9	9.1	0.6	0.94	1.10	-16.513209	64.932716	-16.513205	64.932676
1b	Hot spring	1.7	9.1	9.0	0.5	0.83	0.99	-16.513205	64.932676	-16.513203	64.932635
2	Hot spring	2.4	11.5	8.9	1.08	2.58	3.08	-16.512697	64.932411	-16.512485	64.932362
3	Hot spring	0.3	7.0	9.1	0.27	0.08	0.10	-16.512253	64.930593	-16.512374	64.930549
4	Mixed	1.9	8.4	9.0	0.48	0.92	1.09	-16.514584	64.934238	-16.514668	64.93434
5	Hot spring	0.5	10.9	9.3	0.32	0.15	0.18	-16.517051	64.932611	-16.517029	64.932573
6	Mixed	2.0	9.7	9.1	0.34	0.69	0.82	-16.518366	64.932684	-16.518537	64.932744
7	Mixed	0.9	7.6	9.0	0.16	0.139	0.16	-16.52038	64.932597	-16.520503	64.932654
8	Cold spring	0.2	5.1	9.3	0.17	0.03	0.04	-16.521871	64.932533	-16.52174	64.932545
9	Cold spring	0.1	5.4	9.2	0.31	0.04	0.05	-16.522182	64.932658	-16.522124	64.932683
10	Cold spring	0.3	5.2	9.0	0.39	0.13	0.15	-16.516593	64.934205	-16.516454	64.934226
11	Cold spring	0.6	5.2	9.0	0.49	0.29	0.34	-16.515407	64.934183	-16.515454	64.93414
12	Hot spring	0.7	5.9	9.2	0.88	0.59	0.69	-16.514435	64.932165	-16.514487	64.932195
13	Hot spring	0.5	8.9	9.0	0.62	0.33	0.39	-16.514224	64.932118	-16.514139	64.932108

14	Hot spring	0.7	9.1	9.0	0.20	0.13	0.16	-16.513993	64.931695	-16.513876	64.931695
15	Cold spring	0.2	5.1	9.1	0.35	0.06	0.07	-16.516398	64.933996	-16.51655	64.934083
16	Hot spring	0.3	7.2	9.2	0.33	0.11	0.13	-16.519472	64.93236	-16.519642	64.932379
17	Hot spring	0.5	7.1	9.2	0.33	0.15	0.18	-16.517808	64.932569	-16.517743	64.932625
18	Mixed	1.7	5.8	9.1	0.49	0.83	0.98	-16.513388	64.934368	-16.51351	64.934496
19	Hot spring	0.7	6.5	9.0	0.29	0.20	0.24	-16.513933	64.932489	-16.513998	64.932507
20 a	Cold spring	2.2	5.3	9.2	0.7	1.55	1.81	-16.511968	64.932836	-16.511918	64.932758
20 b	Hot spring	2.7	8.7	9.1	0.8	2.23	2.65	-16.511918	64.932758	-16.51189	64.932717
21	Hot spring	0.1	7.3	9.0	0.46	0.05	0.06	-16.512546	64.93059	-16.512694	64.930596
22	Hot spring	1.0	10.9	9.0	0.73	0.70	0.84	-16.514361	64.930492	-16.514213	64.93048
23	Hot spring	0.6	7.1	9.1	0.35	0.22	0.26	-16.513411	64.930778	-16.513464	64.930739
24	Hot spring	2.5	9.4	9.0	0.71	1.77	2.10	-16.513526	64.930952	-16.513711	64.930995
25	Hot spring	0.3	8.6	9.1	1.01	0.31	0.37	-16.513829	64.93069	-16.513848	64.930625
26 a	Cold spring	1.3	4.5	9.2	0.24	0.31	0.36	-16.513894	64.932708	-16.513882	64.932685
26 b	Hot spring	0.8	5.5	9.2	0.33	0.27	0.32	-16.513882	64.932685	-16.513872	64.93266
27	Cold spring	0.1	5.4	8.8	0.15	0.01	0.01	-16.515392	64.934214	-16.515326	64.934226
28	Glacial	2.6	4.9	8.0	1.13	2.90	3.40	-16.511816	64.929682	-16.511621	64.929597
29	Cold spring	0.0	—*	—*	—*	—*	—*	-16.522133	64.932535	-16.521952	64.932536

1400 *Too shallow for the instruments

1401 B.3. 2018 hydrology analysis

1402 In 2018, we used the same instruments as in 2017; however, having observed during
1403 the preceding years that the channel profiles were generally rectilinear, we simplified our
1404 approach to estimating cross-sectional area by simply calculating it as the product of depth
1405 and width. The only exception to this was the channel described by segments #24 and #25,
1406 which is located where a springwater and lava-filtered spring come together, as shown in Fig.
1407 8c. In this case the channel exhibited a bimodal depth, temperature, and pH distribution, and
1408 we divided it into two segments. Q and E_{flux} were calculated for each channel as before using
1409 Equations 1 and 2.

1410

1411 *Table B3: Results of the field data gathered in the hot springs region on August 11, 2018.*

1412 *Points #16–19 were taken in pools near the lava flow margin, and are not channels. Cross-*

1413 *section #1 has highly variable temperature, velocity, and water levels. See Fig. 6c for a map*

1414 *of these data. Latitude and longitude are referenced to the Islands Net 2004 datum.*

ID	Channel type	Cross-Sectional Area (m ²)	Temperature (°C)	pH	Velocity (m/s)	Discharge Rate (m ³ /s)	Heat Flux (GJ/s)	Start Longitude	Start Latitude	End Longitude	End Latitude
1	Glacial	—*	6.6–10.5	7.7	—*	—*	—*	-16.511357	64.930070	-16.510601	64.929885
2	Hot spring	0.97	9.8	8.8	0.8	0.77	0.92	-16.514314	64.930438	-16.514237	64.930429
3	Cold spring	1.70	3.8	9.1	0.2	0.34	0.40	-16.514331	64.932696	-16.514260	64.932651
4	Hot spring	1.04	7.7	8.9	0.9	0.93	1.10	-16.511398	64.930083	-16.511498	64.930138
5	Hot spring	0.24	7.3	8.8	0.3	0.07	0.08	-16.512179	64.930488	-16.512109	64.930495
6	Hot spring	0.43	7.0	9.0	0.5	0.21	0.25	-16.512320	64.930539	-16.512264	64.930530
7	Hot spring	0.26	7.7	9.8	0.8	0.21	0.25	-16.512625	64.930594	-16.512534	64.930592
8	Hot spring	0.46	7.4	8.9	0.7	0.32	0.38	-16.512843	64.930700	-16.512889	64.930668
9	Hot spring	0.16	7.1	8.8	0.4	0.07	0.08	-16.512987	64.930645	-16.513028	64.930627
10	Hot spring	0.88	7.4	9.1	0.4	0.35	0.42	-16.513410	64.930786	-16.513492	64.930744
11	Hot spring	0.80	7.3	8.9	0.8	0.64	0.76	-16.513684	64.930631	-16.513636	64.930663
12	Hot spring	0.42	7.9	8.9	0.4	0.17	0.20	-16.513648	64.930584	-16.513568	64.930576
13	Hot spring	1.11	7.7	8.8	0.6	0.67	0.79	-16.513532	64.930573	-16.513459	64.930587
14	Hot spring	0.40	8.8	8.9	0.2	0.08	0.10	-16.514091	64.930588	-16.514049	64.930593
15	Hot spring	2.06	9.5	8.9	0.9	1.85	2.21	-16.514122	64.930617	-16.514230	64.930636
16	Hot spring	—**	9.1	8.9	—	—	—	-16.514220	64.930882		
17	Hot spring	—**	8.1	8.9	—	—	—	-16.514031	64.931854		
18	Hot spring	—**	7.7	8.9	—	—	—	-16.514357	64.931841		
19	Hot spring	—**	6.8	9.0	—	—	—	-16.514443	64.931872		
20	Hot spring	0.95	6.4	8.8	0.8	0.76	0.89	-16.514215	64.932133	-16.514101	64.932126
21	Hot spring	0.69	5.5	8.8	1.4	0.97	1.14	-16.514459	64.932204	-16.514396	64.932173
22	Hot spring	1.62	6.7	9.1	0.9	1.46	1.72	-16.513995	64.932326	-16.513935	64.932271
23	Hot spring	3.01	8.2	8.6	0.9	2.71	3.21	-16.513397	64.931490	-16.513041	64.931454

24	Hot spring	0.58	6.6	8.5	0.5	0.29	0.34	-16.513320	64.932666	-16.513296	64.932635
25	Cold spring	2.41	4.8	9.2	0.8	1.93	2.26	-16.513344	64.932708	-16.513320	64.932666

1415 **Too variable to measure*

1416 ***Pool measurement, not transects*

1417